Autonomous Self-Drilling Seed Carriers for Aerial Seeding with Superior Success Rates

Lining Yao (✉ liningy@andrew.cmu.edu)
Carnegie Mellon University
Danli Luo
Carnegie Mellon University
Aditi Maheshwari
Accenture Labs
Andreea Danielescu
Accenture Labs
Jiaji Li
Zhejiang University
Yue Yang
Zhejiang University
Ye Tao
Zhejiang University City College
Lingyun Sun
Zhejiang University
Guanyun Wang
Zhejiang University
Shu Yang
University of Pennsylvania https://orcid.org/0000-0001-8834-3320
Teng Zhang
Syracuse University https://orcid.org/0000-0001-5001-8485

Physical Sciences - Article

Keywords:

Posted Date: February 15th, 2022

DOI: https://doi.org/10.21203/rs.3.rs-1341317/v1

Autonomous Self-Drilling Seed Carriers for Aerial Seeding with Superior Success Rates

Danli Luo[1], Aditi Maheshwari[2], Andreea Danielescu[2], Jiaji Li[3], Yue Yang[3], Ye Tao[4], Lingyun Sun[3], Guanyun Wang[1,3]*, Shu Yang[5]*, Teng Zhang[6,7]*, Lining Yao[1]*

Affiliations

[1]Morphing Matter Lab, Human-Computer Interaction Institute, Carnegie Mellon University, Pittsburgh, PA, United States.

[2]Accenture Labs, San Francisco, CA, United States.

[3]College of Computer Science and Technology, Zhejiang University, Hangzhou, China.

[4]School of Artistic Design and Creation, Zhejiang University City College, Hangzhou, China.

[5]Materials Science and Engineering, University of Pennsylvania, 3231 Walnut Street, Philadelphia, PA 19104, United States.

[6]Department of Mechanical and Aerospace Engineering, Syracuse University, Syracuse, NY, U United States.

[7]BioInspired Syracuse, Syracuse University, Syracuse, NY, United States.

*Correspondence to: guanyun@zju.edu.cn, shuyang@seas.upenn.edu, tzhang48@syr.edu, liningy@andrew.cmu.edu.

Summary:

Aerial seeding can quickly cover large and physically inaccessible areas[1] to improve soil quality and scavenge residual nitrogen in agriculture[2], for postfire reforestation[3–6] and wildland restoration[7,8]. However, it suffers from low germination rates due to the direct exposure of unburied seeds to harsh sunlight, wind, granivorous birds, and undesirable air humidity and temperature[1,9,10]. Inspired by *Erodium* seeds[11–14], we design and fabricate self-drilling seed carriers, turning wood veneer into highly stiff (7.2 GPa when dry, and 1.2 GPa when wet) and hygromorphic bending or coiling actuators with an extremely large bending curvature (1854 m^{-1}),

45 times larger than the literature values[15–18]. Our three-tailed carrier has an 80% drilling success rate on flat land after two triggering cycles due to the beneficial resting angle (25° - 30°) of its tail anchoring, whereas the natural *Erodium* seed's success rate is 0%. Our carriers can carry payloads of different sizes and contents including biofertilizers and plant seeds as large as those of whitebark pine, which are 11 mm in length. We compare experiments with numerical simulation to elucidate the curvature transformation and actuation mechanisms to guide the design and optimization of the seed carriers. Our system will significantly improve the effectiveness of aerial seeding to relieve agricultural and environmental stresses, and has potential applications in energy harvesting, soft robotics and sustainable buildings.

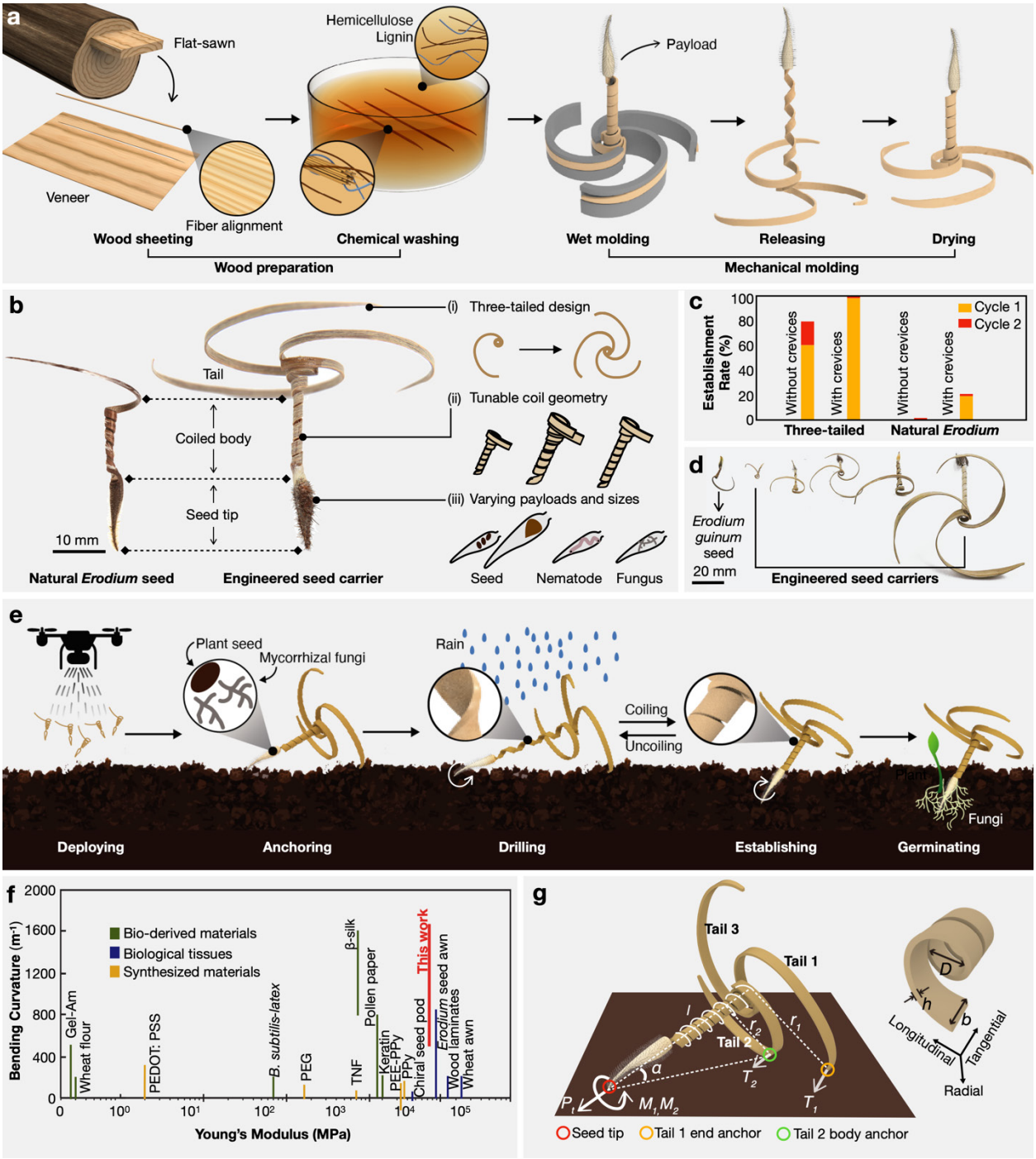

Figure 1. Bioinspired design of the autonomous self-drilling seed carrier. a, The processing steps to create wood-based hygromorphic actuators with a large initial curvature. **a,** The natural *Erodium guinum* seed that serves as our design inspiration. **b,** The natural *Erodium guinum* seed served as the design inspiration, and our design concepts of the autonomous self-drilling seeding carrier with customized awn and tailored payloads. **c**, Our engineered three-tailed seed carrier has

80% higher establishment rates than the *Erodium* seed. Ten three-tailed seed carriers with seven coils and ten *Erodium guinum* seeds were tested in alternating hydration and dehydration cycles of 30 min each. The artificial conical crevice was 3 cm deep. **d**, Engineered and natural seed carriers of different sizes and geometries. **e,** An envisioned application showing a three-tailed carrier delivering vegetable seeds alongside mycorrhizal fungi as symbiotic biofertilizers. **f**, Comparison of our actuator in elastic modulus and bending curvature with typical biological and engineered actuators and materials that exhibit hydration-induced reversible deformation behaviors (see Supplementary Table 1 for additional references and values used to create **f**). **g,** Three-tailed design considerations. Successful drilling relies on the effective vertical thrust force (P_t) and torque (M_1, M_2) that are determined by the moisture-driven mechanics coupled with the wood and the coil's dimensional factors, including the thickness (h), width (b), diameter (D) and the coil's active length (l) and tail configurations.

Main Text:

Natural *Erodium* seeds are known for their self-burial behaviors, where the awn uncoils and coils reversibly in response to variations in external humidity, causing the seed tip to rotate and drill into the ground[11–14]. The self-burial behavior is advantageous, allowing the seed to avoid fire[19], reducing both exposure to high temperature[20] and sensitivity to precipitation and drought. However, *Erodium* seed awns achieved nearly zero anchoring on relatively flat terrain after five triggering cycles in a controlled test (see Supplementary Video 1). Additionally, *Erodium* seed awns have small seedpod sizes (e.g., ~4 mm long from *Erodium cicutarium*, the most common species in North and Central America, carrying seeds of ~2 mm long[11,21]), thus limiting the potential to carry larger payloads such as the 7-11 mm long whitebark pine seeds, which are important for reforestation[22]. An engineered replica of the natural *Erodium* seed has been demonstrated for field sensor deployment[23]. However, a 0 - 20 % establishing rate after the first actuation cycle, limited soil types requiring artificial crevices, and the long chemical washing cycles in manufacturing (7 h) limit its scalability and potential application in aerial seeding. Here, we set three design criteria: (1) They should work robustly on both flat and rough terrains with a high degree of drilling success during the first cycle. (2) The overall size and other geometrical factors are tunable to accommodate payloads up to ~11 mm in length, which covers a wide variety

of seeds from crop seeds to native plant seeds. (3) The materials should be biodegradable and the manufacturing process should be scalable and low-cost.

Taking into consideration the awn topology, the parametric geometries of the tail and coils, and the material's intrinsic properties, we design and fabricate (see Fig. 1a) a three-tailed seed carrier platform from wood veneer, a stiff biomass. The platform (see Fig. 1b) consists of (i) a three-tailed configuration to increase the initial drilling success, (ii) a hygromorphic coiling body with variable geometrical factors that are optimized based on both manufacturability and required thrust force and actuation amplitude, (iii) varying tip and overall sizes to accommodate different payloads. The three-tailed seed carrier performs significantly better than the *Erodium* seed under the same testing conditions, with more noticeable advantages on relatively flat soil (Fig. 1c). Seeds carriers of different sizes and geometrical variations are produced relatively easily (Fig. 1d) to deliver different types of payloads, symbiotic species, and beneficial nematodes. Fig. 1e illustrates an example of a carrier containing both vegetable seeds and mycorrhizal fungi as symbiotic biofertilizers[24] in the same tip for aerial deployment, increasing the potential soil coverage and survival rates. The self-drilling is enabled by natural rain outdoors, achieving a 95% success rate of either establishing or anchoring.

Compared to existing biological and synthetic bending or coiling actuators that exhibit hydration-induced reversible deformation (Fig. 1f), our system has a maximum bending curvature of 1854 m^{-1} that is 45 times larger than that of reported wood-based bending actuators[15–17], and has a fairly large elastic modulus (~7.2 GPa at 20% relative humidity).

Design considerations involving both material and geometrical factors

To effectively drill into the soil, the seed carrier must generate sufficient thrust force (P_t) and torque (M_1, M_2), as shown in Fig. 1g. The thrust force can be expressed as $P_t \sim K\delta$, where δ is the coil axial displacement, and K is the coil spring constant, which is determined by the material's Young's modulus E, and the geometrical parameters of the coil:

$$K \sim Ebh^3\kappa_c^2/l \quad (1)$$

Here, l is the total length of the active coil, b is the width, h is the thickness, and κ_c is the bending curvature (reciprocal to the radius $D/2$ of the coil)[25]. The torques are expressed as $M_1 = r_1 T_1$ and $M_2 = r_2 T_2$, where r_1 and r_2 are the respective distances between tail 1 and tail 2's anchor points on the ground to the coil axis, and T_1 and T_2 are the forces applied at the tails' anchor points due to uncoiling motion of the tails, respectively (Fig. 1g). Additionally, we need to consider the tip rotational speed ω, which is known to reduce the drag force and lower the minimum force needed for drilling[26].

Material choices and processing methods

To drill into natural terrain by harvesting ambient moisture fluctuations, the carrier should be hygromorphic with a large K in both dry and wet states and tightly coiled when dry. Natural wood has well-studied hygromorphic properties[15–18] and is one of the most abundant and environmentally friendly structural materials. Compared to other biodegradable water-responsive materials such as spider silk[27], bacterial spores[28], engineered silk film[29], pollen paper[30], and naturally derived hydrogels[31–34], wood offers superior mechanical strength (E ~10 GPa), and processibility at large scales (from centimeter to meter)[15,16] (see comparison in Supplementary Table 1). However, the high strength limits wood-based actuators with a small initial curvature (< 10 m^{-1}) and limited range of curvature changes (< 30 m^{-1})[15–18]. To tackle this challenge, we develop a five-step process that involves both chemical washing and mechanical molding (see Methods 'Fabrication'), to transform the bulk wood into a tight hygromorphic coiling actuator.

First, white oak lumbers are flat sawn cut (Fig. 1a) for veneer processing as the flat saw does not disrupt the original fiber alignment. White oak is chosen because it has a high tensile modulus E_L (13.5 GPa) along the fiber direction and one of the largest E_T/E_L ratios (0.07, E_T is the modulus along the transverse direction) among common wood types (see Supplementary Table 2 for comparison), which is important to alleviate material failure under large bending deformation in the molding process. The subsequent chemical washing step[35–37] in a boiling bath of sodium hydroxide and sodium sulfite partially removes lignin, thus reducing the strength of wood[35] and making the sheet compliant for mechanical molding[38]. To balance the requirements of high mechanical strength for self-drilling, compliances for wet-molding, and hygromorphic actuation speed and reversibility, our samples are made from the 10-min chemical washing veneer that is

0.5 mm thick, achieving E_L of ~7.2 GPa (dry) and ~1.2 GPa (wet), respectively (see Methods). Similar chemical washing and molding processes have been mostly used to create environmentally durable wood[38], with one exceptional attempt[23] to engineer hygromorphic actuators. However, without understanding its mechanism of curvature formation and analyzing both geometrical and mechanical factors that affect the actuation behaviors, it failed to reveal a reliable design guideline or optimized manufacturing pipeline to yield specific shapes and functions efficiently.

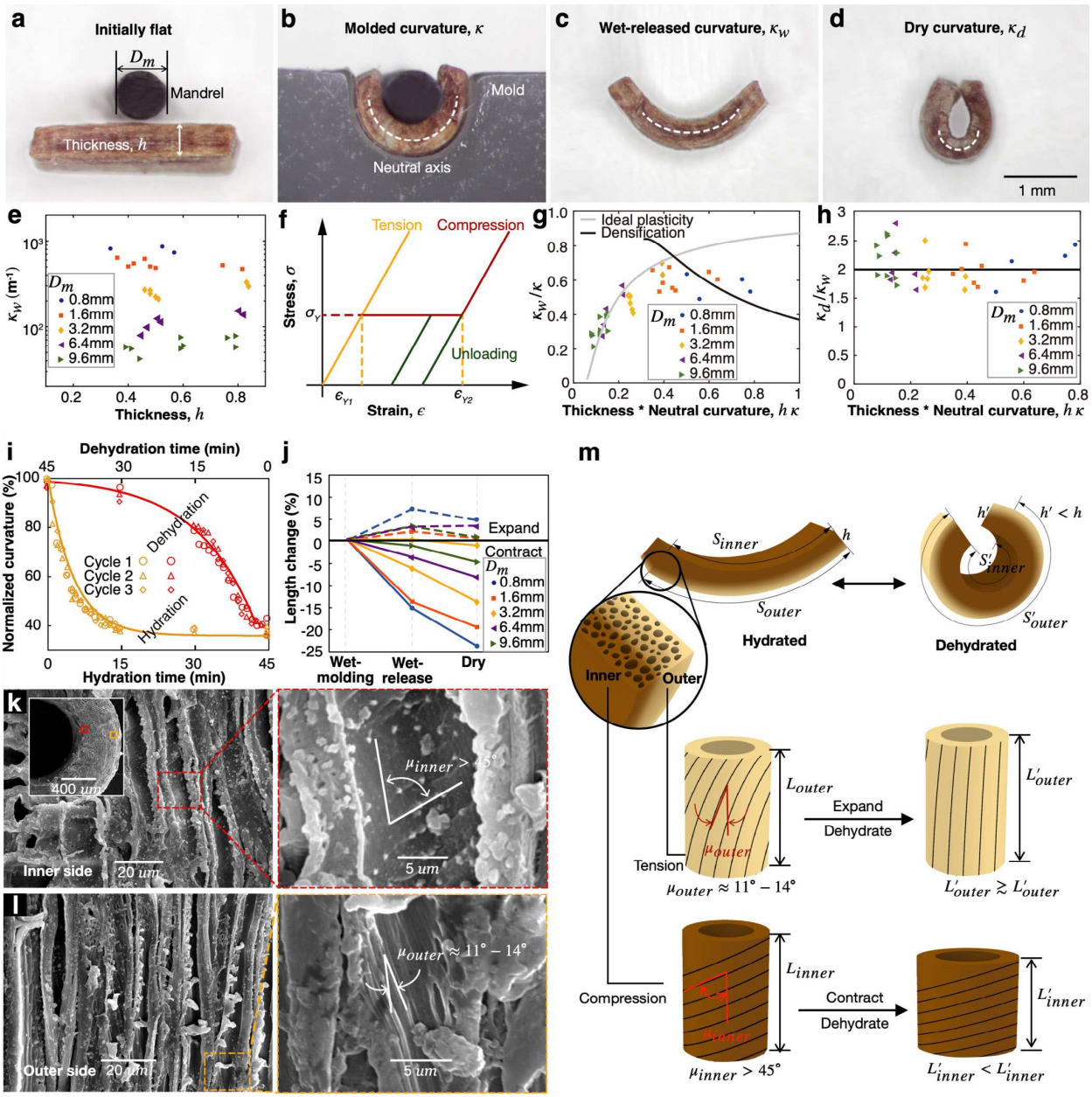

Figure 2. The curvature formation mechanism and hygromorphic actuation. a-d, The curvature changes for .05 mm thick flat wood veneer (**a**) evolves from the as-molded state (**b**) to the wet-released state (**c**) to the dry state (**d**). **e,** The curvature of samples with different thicknesses at the wet-released state after being molded and released from mandrels of varying diameters. **f**, The simplified plastic model with an ideal plastic region ($\epsilon_{Y_1} \leq \epsilon \leq \epsilon_{Y_2}$), followed by a stiffening region ($\epsilon_{Y_2} < \epsilon$). **g,** The normalized curvature in the wet state after release, where κ is the bending curvature with respect to the neutral axis of the sheet during molding. **h**, The normalized curvature

in the dry state. **i,** Reversible curvature changes during three actuation cycles on a sample molded with an 0.8 mm diameter mandrel. **j,** Comparison of length changes of the inner and outer side of the wood strips molded with mandrels of varying diameters. **k-l**, SEM images of the molded and dried wood strip: the cells towards the inner side have wrinkled cell walls and a large microfibril angle (MFA) greater than 45°, and the cells towards the outer side have nearly unchanged cell walls and a smaller MFA of $11° - 14°$. **m**, Illustrations of the curvature formation and actuation mechanisms. The bilayer structure is a simplified model representing the gradient structures in real samples. All samples are 3 mm long, 3 mm wide, and 0.5 mm thick.

Curvature formation and actuation mechanism

The three-step molding process plays a critical role in determining the maximum curvature of the actuator (Fig. 2a-d). While the wet-molding and wet-releasing steps set an initial bending curvature, drying further increases this curvature, leading to a tight coiling. We find that the curvature of the wood veneer at the wet state immediately after the release, κ_w, increases with its thickness, h, from a relatively large diameter mold but decreases with h from a small diameter mold (Fig. 2e). We hypothesize that the curvature κ_w is determined by the plastic deformation accumulated in the molding process. If we assume that plastic deformation only happens under compression on the inner side of the veneer in contact with the mold and adopt a simplified plastic model with an ideal plastic region followed by a stiffening region (Fig. 2f)[38,39], the nonlinear trend can be explained by a beam bending model with asymmetric plastic materials (see Methods 'Curvature analysis A'). Figure 2g shows good agreement between theory and experiments.

As the wet-released wood veneer undergoes drying, the bending curvature further increases, eventually reaching a maximum value κ_d, as the ultimate initial curvature of the actuator (Fig. 2d). The curvature in the wet and dry states are proportional, such that $\frac{\kappa_d}{\kappa_w} \sim 2.0$, as shown in Fig. 2h. The increase of κ_d in the drying step can be attributed to: (1) the decrease along the thickness h direction, and (2) the gradient shrinkage in the longitudinal direction of the veneer. First, h decreases by 20% during dehydration. Based on the reversible actuation in multiple dehydration and hydration cycles (Fig. 2i), we assume that the plastic strain is independent of the moisture-driven shrinkage. Therefore, a reduction in thickness will lead to an increase in the bending

curvature, which is inversely proportional to the thickness ratio, $\frac{\kappa_d}{\kappa_w} = \frac{h}{h'}$, where h' is the thickness of the wood veneer at the dry state (see Methods 'Curvature analysis B').

However, the decrease in thickness cannot account for the total increase in κ_d. Our experiments show that the longitudinal shrinkage exhibits a clear gradient across the thickness direction: the inner edge shrinks by 5% to 23%, while the outer edge expands by 1% to 4%, measured from the bending strips molded with different mandrel diameters (Fig. 2j). Scanning electron microscopy (SEM) images (Fig. 2k-l) show that the cells towards the inner side have a larger microfibril angle (MFA) ($\mu_{inner} > 45°$), while those towards the outer side have a smaller MFA ($\mu_{outer} \approx 11° - 14°$) that is close to the value of the unmodified wood veneer (~10° in Extended Data Fig.1b). The increased μ_{inner} can be attributed to the stress induced fiber alignment[40]. Based on the Fratzl–Elbaum–Burgert model[41,42], along its longitudinal direction, the wood cell will expand when the MFA is larger than 45° and remain relatively unchanged when the MFA is around 11° during hydration. Therefore, the large μ_{inner} contributes to the elongation of the inner side along the strip and the smaller μ_{outer} contributes to an almost stress-free outer side with negligible expansion when hydrated. The gradient MFAs in combination with the reversible changes in thickness h not only contribute to the initial molding curvature κ_d but also explain the reversible curvature changes during actuation cycles, as illustrated in Figure 2m. This is experimentally validated in three consecutive actuation cycles with a 98% and 85% recovery of the initial curvatures for bending and coiling actuators, respectively (See Methods 'Bending angle measurement' and Extended Data Fig. 2).

Combining the effects of the shrinkages along the radial (across the thickness) and longitudinal directions, the dry curvature can be expressed as $\frac{\kappa_d}{\kappa_w} = \frac{h}{h'}(1 + \beta)$, where β describes the coupling between the mechanical strain and shrinkage. This theoretical prediction fits the experimental data well when $\beta = 0.6$ (Fig. 2h).

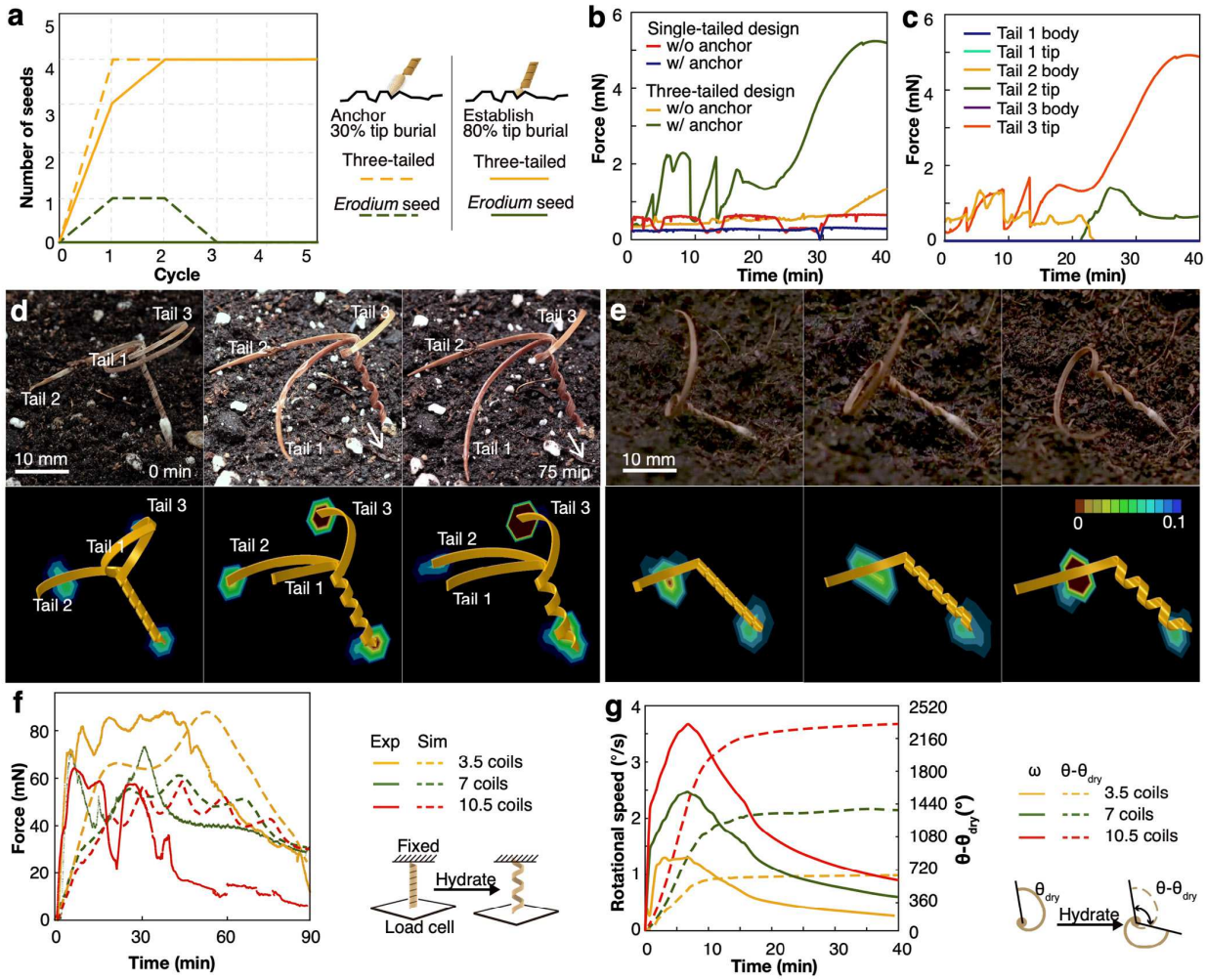

Figure 3. Geometrical parameters of the seed carrier design. a, Comparison of drilling success between the engineered three-tailed seeds and natural *Erodium* seeds on a relatively flat soil. **b,** Comparison of simulated thrust force between the seed tip and the ground from the three-tailed and the single-tailed designs. **c,** Finite element simulation results of the dynamic forces generated by multiple tail bodies and tips as the three-tailed seed touches the ground. **d-e,** Experimental (top) and simulation (bottom) results of three-tailed (**d**) vs. single-tailed (**e**) seed carriers, during the first hydration cycle triggered by natural rain outdoors. For the three-tailed design shown in **(d)**, the body of tail 2 and the tip of tail 3 generate forces initially, then both tips of tail 1 and 2 start to generate larger forces as the tails get more hydrated. In contrast, the force stays relatively constant and small for the single-tailed design in **(e)**. The color bar represents the contact pressure (unit kPa). **f,** Comparison of peak extension force of coiling actuators with different coiling numbers

and total length in both experiments and simulation. **g,** Comparison of rotational speed of coiling actuators with different coiling numbers and total length in experiments.

Geometrical parameters that affect the drilling success rate

The drilling success rate is highly dependent on the thrust force, the torque, and the landing pose of the seed carrier. First, the topology of the three-tail arrangement helps secure an initial angle (α) between the tip and ground (Fig. 1g), which is critical to generating effective torque and thrust force to increase the chance of successful drilling. When dropped on the soil 30 times from 0.3 m above the surface in an indoor controlled test, *Erodium* seeds have an 80% chance to land flat ($\alpha = 0$), while the three-tailed carrier has a 90% chance of landing at an angle between 25° to 30° (Supplementary Video 2). Drone deployment of the three-tailed seed carriers from 5 to 6 m above ground results in a 90% success rate of landing at a beneficial initial angle (Extended Data Fig. 3). A subsequent self-drilling test shows that four out of five three-tailed seed carriers successfully established tip burial after two hydration-dehydration cycles, while none of the single-tailed carriers establishing after five cycles (Fig. 3a, Supplementary Video 3, and Methods 'Drilling tests under controlled conditions'). To better understand the roles of the geometric parameters of the coil and the mechanical properties of the wood material, we conduct finite element (FE) simulations to predict the coiling actuator performance (see Methods). As seen from Fig. 3b-e and Supplementary Video 4, the three-tailed design generates a much larger thrust force than the single-tailed one since each tail may anchor and they generate effective torques simultaneously in contrast to the single torque generated by the single tail's body.

Besides the number of tails, the stiffness of the coil (K) also plays a critical role in determining the thrust force. To quantify how the length of the active coiled body, l, affects the extension force P_e, we measure P_e with varying total numbers of coils. Fig. 3f and Extended Data Fig. 4a show that the fewest number of coils (3.5) measured has the largest peak force, 90 mN, which is twice as large as that of the natural *Erodium* seed with the same number of coils (43 mN). The peak force can be further increased using a double-layer body (Extended Data Fig. 4b). The extension force profile obtained from FE analysis (Fig. 3e) matches well with experiments.

In addition to tail configuration and coil stiffness, increasing the rotational speed ω of the coiled body will reduce the drag force between the tip and the soil, facilitating drilling[26]. While increasing the total number of coils increases ω (Fig. 3g), it also decreases the generated extension force P_e.

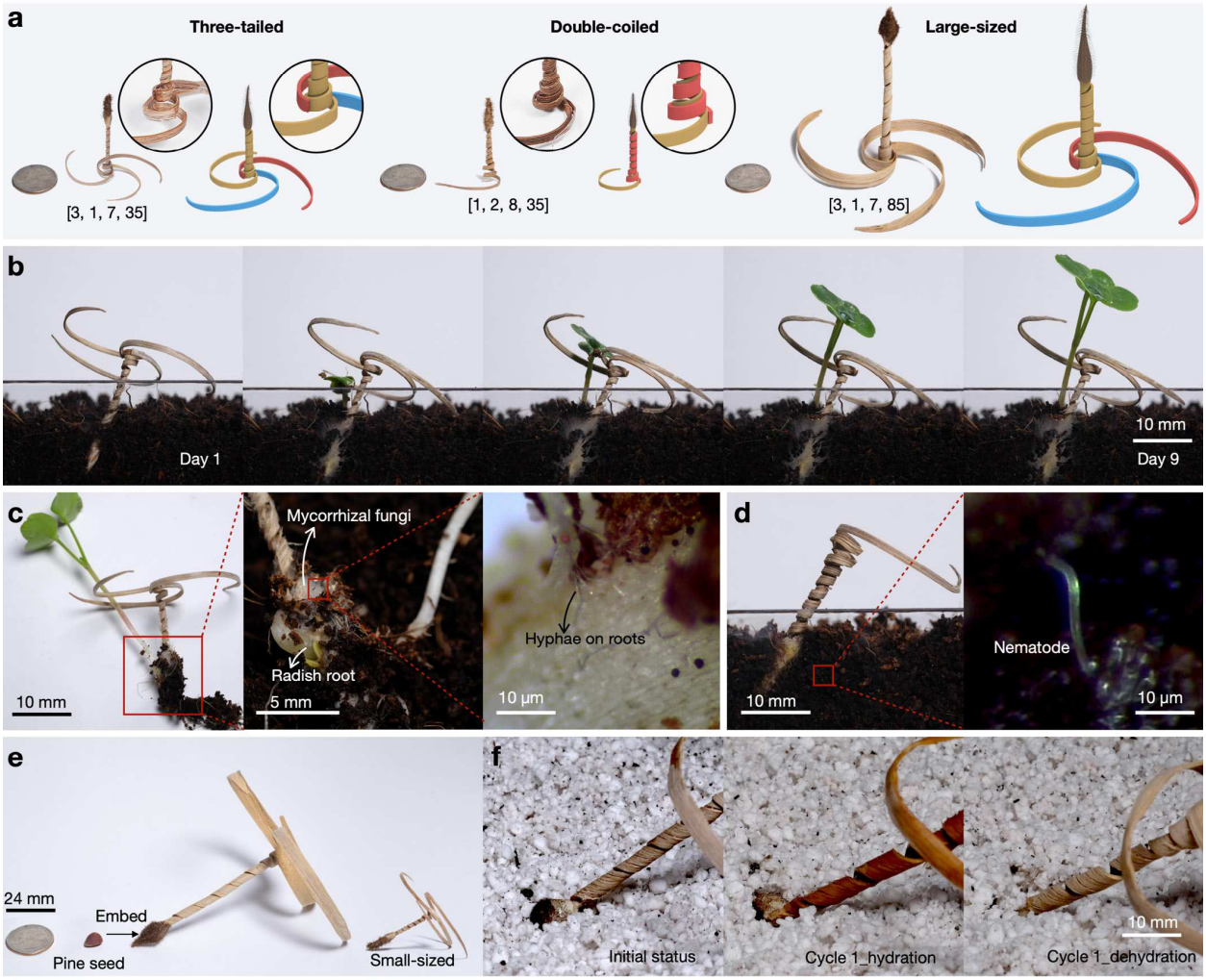

Figure 4. Tailored designs of self-drilling carriers. a, Three different engineered seed carrier designs with different size, coil, and tail variations. The identifying numbers beneath each case indicate: (i) the total number of tails, (ii) the total layers of the coiled body, (ii) the total numbers of coils, and (iv) the total body length in mm. **b,** The germination process of a three-tail seed carrier with embedded symbiotic species: cherry belle radish seeds and mycorrhizal fungi. **c,** The symbiotic growth of radish seeds and mycorrhizal fungi. **d,** Nine days after delivery of beneficial nematodes, *Steinernema carpocapsae*, that prefer growing in the dark by a double-coiled seed carrier. **e,** A large-sized seed carrier is designed to carry whitebark pine seed for reforestation. **f,**

The successful drilling of the large-sized seed carrier with a whitebark pine seed after the first triggering cycle. Drilling tests in (**b-d)** used four triggering cycles on coconut coir soil. The subsequent germination and incubation experiments lasted for nine days under 25°C and 40% relative humidity. The test in (**f)** used one triggering cycle on a perlite bed. More details for tests (**b-d**, **f**) are included in the Methods.

Tailored seed carrier designs for different terrains and seed types in controlled tests

The geometric-based designs allow us to tailor the self-drilling seed carriers for different terrain conditions and seed types for different applications (Fig. 4a, and Supplementary Video 5). The process to integrate different payloads is shown in Extended Data Figure 5 and Supplementary Video 6, and the drilling test conditions are described in the Methods. First, two symbiotic species – two cherry belle radish seeds and 1 mg of mycorrhizal fungi as a soil nutrient – embedded within one tip were successfully deployed in coconut coir soil after four triggering cycles. After nine days, the seeds germinated and the fungi was visible near the plant roots under a light microscope (Fig. 4b, c, and Supplementary Video 7).

We then tested the delivery of beneficial nematodes, *Steinernema carpocapsae*, which improve plant health[43] but require deeper burial since nematodes like to grow in a dark environment[44]. In order to increase the drilling depth we engineered a double-coiled seed carrier (Fig. 4d). As seen in Extended Data Figure 6, the single coiled bodies achieved a tip depth of 13.5-16.5 mm tip while the double-coiled one achieved a tip depth of 16.5-18 mm after four self-burial triggering cycles. After nine days, we observed a proliferation of the nematodes in the surrounding coconut coir soil.

To carry larger seeds (e.g., seeds of whitebark pine, a candidate keystone species under the Endangered Species Act and a common target of reforestation efforts in the United State and Canada[45–47]), we fabricated a large-sized seed carrier with a full body length of 85 mm (Fig. 4e). The whitebark pine seeds showed successful self-burial on a perlite bed within the first hydration-dehydration cycle of one hour (Fig. 4f).

Drilling test under natural stimuli

We further carried out self-drilling tests by dropping 22 three-tailed seed carriers in an open field in Pittsburgh, PA, USA, with the soil having a 4.61 $\log_{10}$ soil microtopographical variance (Extended Data Fig. 7). The test was conducted in early July 2021, with two intermittent light rains on the first day and one thunderstorm and heavy rain lasting for more than six hours on the second day. The seed carriers had high drilling efficiency after two lighter rains with a 95% success rate of either establishing or anchoring. Then, the heavy thunderstorm on the second day dislodged 80% of the previously anchored yet not fully established seed carriers. After the rain stopped on day three, the flattened seed carrier tails were recovered on the previously flooded raised beds, suggesting that the tails could continue attempting to drill in subsequent rain cycles. Most of the seed tips, however, were damaged by the flood, preventing them from further drilling. Nearly half of the non-dislodged ones were able to germinate after five to seven days in the open environment without human intervention (Supplementary Video 8). While our current study focuses on optimizing the seed body (coil and tail) design and has validated its effectiveness in natural conditions, we expect to further optimize the seed tip engineering[23] to further improve the tip's resilience to harsh environments and hostile climate effects such as extreme flooding or drought.

Conclusion

We have designed and engineered three-tailed seed carriers from low-cost, scalable, and biodegradable wood veneer that can self-drill into the ground in response to moisture fluctuations in the environment. We present key design principles to improve the success rate of self-drilling and elucidate the actuation mechanisms by investigating the geometric factors and intrinsic material properties through both simulation and experiments. Our carrier can be tailored for quick deployment of seeds, microorganisms and other soil nutrients through aerial delivery, with promising implications for agriculture, reforestation and natural conservation in environmentally degraded regions. Combined with other technologies – for example, embedding fertilizers[48] and soil sensors[23] in the carrier's tip or body for precision farming – our seed carriers will potentially help to relieve the agricultural stress from global warming. Lastly, the general approach of processing wood into actuators with a large initial curvature and amplitude may find broader

applications in energy harvesting[49], biodegradable hydromorphic robotics[50] and sustainable responsive architecture[17].

References

1. Fisher, K. A., Momen, B. & Kratochvil, R. J. Is broadcasting seed an effective winter cover crop planting method? *Agron. J.* **103**, 472–478 (2011).
2. Ball, B. C. Cereal production with broadcast seed and reduced tillage: a review of recent experimental and farming experience. *J. Agric. Eng. Res.* **35**, 71–95 (1986).
3. Kelly, L. T. *et al.* Fire and biodiversity in the Anthropocene. *Science* **370**, (2020).
4. Grose, R. J., Moulds, F. R. & Douglas, M. G. Aerial seeding of alpine ash. *Aust. For.* **28**, 176–186 (1964).
5. Keane, R. E. Managing wildfire for whitebark pine ecosystem restoration in western North America. *Forests* **9**, 648 (2018).
6. Xiao, X. *et al.* Aerial seeding: an effective forest restoration method in highly degraded forest landscapes of sub-tropic regions. *Forests* **6**, 1748–1762 (2015).
7. Monsen, S. B., Stevens, R. & Shaw, N. L. *Restoring western ranges and wildlands*. 1–294 https://www.fs.usda.gov/treesearch/pubs/7377 (2004).
8. U.S. Fish & Wildlife Service. Marsh restoration. https://www.fws.gov/refuge/Prime_Hook/what_we_do/marshrestoration.html (2020).
9. Collins, B. A. & Fowler, D. B. A comparison of aerial and conventional methods for seeding winter wheat. (1989).
10. Keisling, T. C., Dillon, C. R., Oxner, M. D. & Counce, P. A. An economic and agronomic evaluation of selected wheat planting methods in Arkansas. *Partn. A* 156 (1997).
11. Stamp, N. E. Self-burial behaviour of Erodium cicutarium seeds. *J. Ecol.* **72**, 611–620 (1984).
12. Ha, J. *et al.* Hygroresponsive coiling of seed awns and soft actuators. *Extreme Mech. Lett.* **38**, 100746 (2020).
13. Almeida, A. P. C. *et al.* Reversible water driven chirality inversion in cellulose-based helices isolated from Erodium awns. *Soft Matter* **15**, 2838–2847 (2019).
14. Abraham, Y. *et al.* Tilted cellulose arrangement as a novel mechanism for hygroscopic coiling in the stork's bill awn. *J. R. Soc. Interface* **9**, 640–647 (2012).
15. Rüggeberg, M. & Burgert, I. Bio-inspired wooden actuators for large scale applications. *PloS One* **10**, e0120718 (2015).
16. Grönquist, P. *et al.* Analysis of hygroscopic self-shaping wood at large scale for curved mass timber structures. *Sci. Adv.* **5**, eaax1311 (2019).
17. Holstov, A., Bridgens, B. & Farmer, G. Hygromorphic materials for sustainable responsive architecture. *Constr. Build. Mater.* **98**, 570–582 (2015).

18. Krieg, O. D. HygroSkin – Meteorosensitive Pavilion. in *Advancing wood architecture: a computational approach* (eds. Achim, M., Schwinn, T. & Krieg, O. D.) 16 (Routledge, Taylor & Francis Group, 2016).
19. Tothill, J. C. Soil temperatures and seed burial in relation to the performance of Heteropogon contortus and Themeda australis in burnt native woodland pastures in eastern Queensland. *Aust. J. Bot.* **17**, 269–275 (1969).
20. Rice, K. J. Responses of Erodium to Varying Microsites: The Role of Germination Cueing. *Ecology* **66**, 1651–1657 (1985).
21. Mensing, S. & Byrne, R. Pre-mission invasion of Erodium cicutarium in California. *J. Biogeogr.* **25**, 757–762 (1998).
22. Keane, R. E. *et al. A range-wide restoration strategy for whitebark pine (Pinus albicaulis)*. 108 https://www.fs.usda.gov/treesearch/pubs/40884 (2012).
23. Luo, D., Gu, J., Qin, F., Wang, G. & Yao, L. E-seed: shape-changing interfaces that self drill. in *Proceedings of the 33rd Annual ACM Symposium on User Interface Software and Technology* 45–57 (Association for Computing Machinery, 2020). doi:10.1145/3379337.3415855.
24. Igiehon, N. O. & Babalola, O. O. Biofertilizers and sustainable agriculture: exploring arbuscular mycorrhizal fungi. *Appl. Microbiol. Biotechnol.* **101**, 4871–4881 (2017).
25. Jung, W., Kim, W. & Kim, H.-Y. Self-burial mechanics of hygroscopically responsive awns. *Integr. Comp. Biol.* **54**, 1034–1042 (2014).
26. Jung, W., Choi, S. M., Kim, W. & Kim, H.-Y. Reduction of granular drag inspired by self-burrowing rotary seeds. *Phys. Fluids* **29**, 041702 (2017).
27. Agnarsson, I., Dhinojwala, A., Sahni, V. & Blackledge, T. A. Spider silk as a novel high performance biomimetic muscle driven by humidity. *J. Exp. Biol.* **212**, 1990–1994 (2009).
28. Chen, X., Mahadevan, L., Driks, A. & Sahin, O. Bacillus spores as building blocks for stimuli-responsive materials and nanogenerators. *Nat. Nanotechnol.* **9**, 137–141 (2014).
29. Park, Y. *et al.* β-Sheet nanocrystals dictate water responsiveness of bombyx mori silk. *Macromol. Rapid Commun.* **41**, 1900612 (2020).
30. Zhao, Z. *et al.* Digital printing of shape-morphing natural materials. *Proc. Natl. Acad. Sci.* **118**, e2113715118 (2021).
31. Shintake, J., Sonar, H., Piskarev, E., Paik, J. & Floreano, D. Soft pneumatic gelatin actuator for edible robotics. in *2017 IEEE/RSJ International Conference on Intelligent Robots and Systems (IROS)* 6221–6226 (IEEE, 2017). doi:10.1109/IROS.2017.8206525.
32. He, Q., Huang, Y. & Wang, S. Hofmeister effect-assisted one step fabrication of ductile and strong gelatin hydrogels. *Adv. Funct. Mater.* **28**, 1705069 (2018).
33. Baumgartner, M. *et al.* Resilient yet entirely degradable gelatin-based biogels for soft robots and electronics. *Nat. Mater.* **19**, 1102–1109 (2020).
34. Zhao, D. *et al.* High-strength and high-toughness double-cross-linked cellulose hydrogels: a new strategy using sequential chemical and physical cross-linking. *Adv. Funct. Mater.* **26**, 6279–6287 (2016).

35. Song, J. *et al.* Processing bulk natural wood into a high-performance structural material. *Nature* **554**, 224–228 (2018).
36. Frey, M. *et al.* Delignified and densified cellulose bulk materials with excellent tensile properties for sustainable engineering. *ACS Appl. Mater. Interfaces* **10**, 5030–5037 (2018).
37. Frey, M. *et al.* Tunable wood by reversible interlocking and bioinspired mechanical gradients. *Adv. Sci.* **6**, 1802190–1802190 (2019).
38. Xiao, S. *et al.* Lightweight, strong, moldable wood via cell wall engineering as a sustainable structural material. *Science* **374**, 465–471 (2021).
39. Holmberg, S., Persson, K. & Petersson, H. Nonlinear mechanical behaviour and analysis of wood and fibre materials. *Comput. Struct.* **72**, 459–480 (1999).
40. Zhang, Y. *et al.* Molecular insights into the complex mechanics of plant epidermal cell walls. *Science* **372**, 706–711 (2021).
41. Fratzl, P., Elbaum, R. & Burgert, I. Cellulose fibrils direct plant organ movements. *Faraday Discuss.* **139**, 275–282 (2008).
42. Quan, H., Kisailus, D. & Meyers, M. A. Hydration-induced reversible deformation of biological materials. *Nat. Rev. Mater.* **6**, 264–283 (2021).
43. Goodrich-Blair, H. They've got a ticket to ride: Xenorhabdus nematophila–Steinernema carpocapsae symbiosis. *Curr. Opin. Microbiol.* **10**, 225–230 (2007).
44. Gaugler, R. & Boush, G. M. Effects of ultraviolet radiation and sunlight on the entomogenous nematode, Neoaplectana carpocapsae. *J. Invertebr. Pathol.* **32**, 291–296 (1978).
45. Keane, R. E. & Parsons, R. A. *Management guide to ecosystem restoration treatments: Whitebark pine forests of the northern Rocky Mountains, U.S.A.* 133 https://www.fs.usda.gov/treesearch/pubs/34699 (2010).
46. Keane, R. E. *et al. A range-wide restoration strategy for whitebark pine (Pinus albicaulis)*. RMRS-GTR-279 https://www.fs.usda.gov/treesearch/pubs/40884 (2012) doi:10.2737/RMRS-GTR-279.
47. Pansing, E. R. & Tomback, D. F. Survival of Whitebark Pine Seedlings Grown from Direct Seeding: Implications for Regeneration and Restoration under Climate Change. *Forests* **10**, 677 (2019).
48. Aziz, T. *et al.* Fertilizers and environment: issues and challenges. in *Crop Production and Global Environmental Issues* (ed. Hakeem, K. R.) 575–598 (Springer International Publishing, 2015). doi:10.1007/978-3-319-23162-4_21.
49. Park, Y. & Chen, X. Water-responsive materials for sustainable energy applications. *J. Mater. Chem. A* **8**, 15227–15244 (2020).
50. Shin, B. *et al.* Hygrobot: A self-locomotive ratcheted actuator powered by environmental humidity. *Sci. Robot.* **3**, eaar2629 (2018).

Methods

Fabrication

The five-step approach involves the processing of bulk wood into wood veneers with suitable dimensions, the partial removal of lignin and hemicellulose via a short boiling process in an aqueous mixture of sodium hydroxide (NaOH) and sodium sulfite (Na_2SO_3) to improve the moldability of the wood veneer, followed by three-step mechanical molding including a wet molding, a releasing and a drying step.

Wood veneer processing. 3 cm-thick white oak (*Quercus alba*) lumber is acquired from a local lumberyard in North America and prepared in-house. The lumber is flat-sawn into a block with dimensions of roughly 20 cm by 40 cm with the long edge being parallel to the fiber direction. The block is then sliced into four to five thin sheets, each running through a drum sander to further reduce the thickness until it reaches the desired value. The wood veneers obtained after this step have a range of thickness from 0.4 mm to 0.8 mm. All the test samples and application examples are outlined in Rhinoceros. The outlines are sent to a laser cutter (Universal Laser Systems) and cut from the wood veneer with required thickness. Before cutting, the exact location of the outlines is visually inspected to avoid tree rings and Medullary rays in white oak.

Chemical washing. In this step, sodium hydroxide (NaOH, Innovating Science, laboratory-grade), sodium sulfite (Na_2SO_3, LabChem, ACS grade), and filtered water are used for partial delignification chemical baths. The obtained wood strips are immersed in a boiling aqueous solution of 2.5 M NaOH and 0.4 M Na_2SO_3 for different durations specified in each test (Extended Data Fig. 5e), followed by rinsing in boiling water with gentle agitation three times until water was clear.

Mechanical molding. For making coiling actuators, the chemically washed veneer strips are pat-dried on a paper towel and sit in open air for 1 min before molded tightly on a 3D-printed mold (by Formlabs 3, Extended Data Fig. 5f and g). The body coiling diameter can be varied by inserting mandrels of varying diameters into the mold. The molded wood veneer is released from the mold when still wet, and dry at room temperature for 12 h (Extended Data Fig. 5h to j).

Tip fabrication (Extended Data Fig. 5n-t). For the fully biodegradable seed carrier, the tip is made of a dough by mixing 42 g flour and 112 mL water, shaped by a two-part mold. After the dough dries completely after 12 h, the tip is dipped in a 20 wt% ethyl cellulose/ethanol solution twice for waterproofing following the literature procedure[23]. Immediately after the second dip, the tip is coated with a uniform layer of horse mane hairs cut into 2 mm fibers by electrostatic flocking.

The three-tailed seed carriers are made with two separately molded tails that are glued to the end of the active coil (Extended Data Fig. 5k, m). The double-coil seed carriers are made with an additional layer of washed wood veneer molded around the first layer of the coiling body, and both layers are clamped to dry for 12 hours. The large-sized seed carrier is made of a wood veneer with 0.8 mm thickness, 12 mm width, and 300 mm length, molded around a mandrel with 3 mm diameter. Two extra tails are glued at the end of the active coil. A whitebark pine seed (Pinus albicaulis) is embedded inside the flour dough tip and hairs are then added.

For making bending actuators in Fig. 2 with the mentioned five-step process, the washed veneer strips are molded against the mandrel (convex) with an acrylic-based negative mold (concave) on the outer peripheral. The size of the mandrel and the acrylic mold varied based on the desired bending curvature and sample thickness.

Optimization of the chemical washing parameters

We conduct sequential experiments to optimize the processing parameters. The Young's modulus of the wood veneer of 0.5 mm thickness starts to decrease as the duration of chemical washing is increased beyond 10 min (Extended Data Fig. 8a). To measure the Young's modulus of different treated wood veneers, tensile tests are performed on an Instron 5500R using a 500 lb load cell. The dimensions of the test samples are 4 mm wide by 40 mm long by 0.5 mm thick. The samples are clamped at both ends and stretched at a speed of 0.05 inch/min along the fibril direction of the wood until the sample fractured. The modulus of each sample is calculated from the slope of the linear regime. A shorter washing duration (5 min) results in a smaller initial curvature and less recovery after one actuation cycle (Extended Data Fig. 8b). In addition, with the same chemical washing duration of 10 min, the molding starts to fail as the wood veneer exceeded 0.8 mm in thickness (Extended Data Fig. 8c).

Peak force measurement

The extension force of coils with different length is measured in a customized humidity chamber of 20 cubic cm (Extended Data Fig. 4c). A load cell with a capacity of 100 g (TAL221, HTC sensors) is connected to a signal amplifier (HX 711, Sparkfun). A combined temperature and humidity sensor (SHTC3, Sparkfun) is placed inside the chamber to monitor the conditions. A mixture of hot steam and ultrasonic-generated mist is fed into the chamber constantly during all hydration processes. The temperature and relative humidity are kept at 30°C and 100% during hydration that lasts for 90 mins until the sample is fully hydrated and the curvature would not change further. The force measurement would stay constant for prolonged hydration beyond 90 mins. During dehydration, the temperature is kept at 25°C with the relative humidity in the range of 30~40% for another 30 mins until the sample shortens to detach from the measuring plate and the measurement dropped to zero. For dehydration processes, the mist is shut off and a fan is turned on to promote ventilation.

Bending angle measurement

We measure bending angles of both bending (Fig. 2a-j) and coiling (Fig. 3f) actuators in multiple cycles, to understand the actuation amplitude, speed and recovery. Each actuator undergoes multiple hydration and dehydration cycles. The hydration processes are conducted in a water tank. The water in the tank is kept at 25°C. During dehydration processes, the samples are taken out from the water tank and kept at 25°C with the relative humidity in the range of 30~40%. The images used in the analyses are taken by a camera (XT-1, Fujifilm) with a macro lens (XF 60mm f/2.4 R, Fujifilm).

Drilling tests under controlled conditions

The lab setting consists of a timed misting (for hydration) and heated fan (for dehydration and air circulation) mounted above a 50 cm by 50 cm testing area covered by a single layer of cobblestones underneath a 10 cm layer of perlite (Miracle-Gro). We measure the surface roughness by a pin method adapted from literature[51] (Extended Data Fig. 7c). Ten pins with a separation of 1 cm from each other are placed on three sections on each bed. The $\log_{10}$ soil microtopographical

variance is calculated as the variance of the vertical pin heights against a measuring board. Our perlite bed has a 0.78 $\log_{10}$ soil microtopographical variance.

For natural *Erodium* seed and engineered single-tailed seed carriers with both single-coiled and double-coiled bodies, the soil is textured with a 3 cm-deep conical crevice to facilitate the drilling process for parallel comparison. For other drilling tests including the three-tailed drilling and large-sized seed drilling tests, no crevices are introduced. For all the self-drilling tests, four cycles of hydration-dehydration lasting for four hours are performed, while the surface temperature of the soil is kept at ~ 30°C. Alternating misting and drying cycles of 30 minutes each are conducted. Water is supplied at 70 psi through six brass misting nozzles with an orifice of 0.3 mm (Aootech) to simulate misting, and fanned warm airflow from two electric space heaters (Douhe) is supplied to simulate drying.

Drilling tests under natural conditions

The field tests are performed in three raised beds (2 m by 1 m) outdoors containing regular potting soil. After conducting a standard sowing process, we measure the soil roughness[51] (Extended Data Fig. 7c). The $\log_{10}$ soil microtopographical variance is 4.61. The test was conducted in early July 2021 in Pittsburgh in the US, with an average temperature of 17 – 29 Celsius, wind speed of 2 – 11mph and relative humidity of 10% – 100%. All the artificial seed carriers were dropped from a 30 cm height above the surface of the soil with at least 10 cm separation. There was no rain when the seeds were dropped, with two subsequent intermittent light rains on the first day followed by one severe thunderstorm and heave rain lasted for more than six hours on the second day.

Germination and incubation

In the indoor germination and incubation experiments, coconut coir (Mountain Valley Seed Co.) is used as the soil. Four cycles of hydration-dehydration are performed following the standard protocol developed for the drilling tests under controlled conditions. The self-anchored seed carriers are then left in soil for nine days, while the soil is kept moist during the experiments under 25°C and 40% relative humidity.

The germination and microbe-delivery experiments are conducted with the fully biodegradable tips made of flour. An additional 10% w/w mycorrhizal fungi (Mikro-myco, mixture of Endo Mycorrhizae (260 cfu/g), Ecto Mycorrhizae (218,000 cfu/g), Trichoderma (750,000 cfu/g), and Bacillus (400,000,000 cfu/g) is mixed into the flour to make the dough that is molded into the seed tip. Two cherry belle radish seeds (Eden Brothers, USA) are embedded inside the dough. The dough is then air dried for 12 h before adding the hairs. In the microbe-delivery experiment, nematode powder (Steinernema feltiae, BioLogic Scanmask) is mixed into the dough at 10% wet dough weight for making the tip.

Curvature analysis

A. Curvature in the wet sate just after release. Under scanning electron microscopy (SEM) (Extended Data Fig. 1a), after molding, irreversible deformation such as cell wall corrugation and bulges due to compression are observed on the inner side but not the outer side. Therefore, we assume that plastic deformation only happens under compression and adopt a simplified plastic model with an ideal plastic region followed by a stiffening region (Fig. 2f)[39,52]. The plastic strain is governed by two critical parameters, ϵ_{Y_1} and ϵ_{Y_2}, defining the boundary of the ideal plastic region and stiffening region, respectively (Fig. 2f). Plastic deformation is accumulated in the inner region of the veneer in the molding process. Upon release, the elastically deformed outer layer will tend to retract to its original flat shape and thus bend the plastically deformed and curved inner portion of the veneer, resulting in an intrinsic curvature of wood veneers at the wet-released state, κ_w (Fig. 2c), which can be obtained through analyzing the competition between the elastic recovery and accumulated plastic deformation (Supplementary Note 1). For wood veneers within the ideal plastic deformation region, κ_w can be expressed as

$$\frac{\kappa_w}{\kappa} = \left(\frac{1}{2} + 2\left(-\frac{1}{2} + \sqrt{\frac{2\epsilon_{Y_1}}{\kappa h}} \right)^3 - \frac{3}{2}\left(-\frac{1}{2} + \sqrt{\frac{2\epsilon_{Y_1}}{\kappa h}} \right) \right) \quad (1)$$

where κ is the bending curvature respect to the neutral axis during the molding process and given by

$$\kappa = \frac{4\left(1-\epsilon_{Y_1}\right)^2}{\left(\sqrt{2\epsilon_{Y_1}h+4(R+h)\left(1-\epsilon_{Y_1}\right)}-\sqrt{2\epsilon_{Y_1}h}\right)^2}. \quad (2)$$

Equation (1) shows that wood veneers with different thickness and mold curvatures will follow a master curve, which is validated by our experimental data (Fig. 2g).

For wood veneers within the stiffening deformation region, κ_w can be written as

$$\frac{\kappa_w}{\kappa} = 3\frac{(\epsilon_{Y_2}-\epsilon_{Y_1})}{\kappa h}\left(1-4\left(\frac{y_4}{h}\right)^2\right)+\left(4\left(\frac{y_4}{h}\right)^3+2\left(\frac{y_2}{h}\right)^3-6\frac{y_2}{h}\left(\frac{y_4}{h}\right)^2\right), \quad (3)$$

where $\frac{y_2}{h} = \frac{y_1}{h} + \frac{\epsilon_{Y_1}}{\kappa h}$ and $\frac{y_4}{h} = \frac{y_1}{h} + \frac{\epsilon_{Y_2}}{\kappa h}$ and κ and y_1 are given by

$$\kappa = \frac{\frac{R}{h}(\epsilon_{Y_2}-\epsilon_{Y_1})+1\sqrt{\left(\frac{R}{h}(\epsilon_{Y_2}-\epsilon_{Y_1})+1\right)^2-4\left(\frac{R}{h}+\frac{1}{2}\right)\left((\epsilon_{Y_2}-\epsilon_{Y_1})-\frac{1}{2}\left(\epsilon_{Y_2}^2-\epsilon_{Y_1}^2\right)\right)}}{2R+h}, \quad (4)$$

and

$$y_1 = \left(\kappa h+\epsilon_{Y_1}-\epsilon_{Y_2}\right)^{-1}\left(\frac{1}{2\kappa}\left(\epsilon_{Y_2}^2-\epsilon_{Y_1}^2\right)-\frac{h}{2}\left(\epsilon_{Y_2}-\epsilon_{Y_1}\right)\right). \quad (5)$$

Equation (3) also shows that wood veneers with different thickness and mold curvatures will follow a master curve, which is validated by our experimental data (Fig. 2g).

Note that we neglect the modulus reduction and irreversible deformation near the outer layer due to local fiber damages, which is not expected to lead to significant changes as the current model can already match with experiments well.

B. Curvature in the dry state. Our experiments show the thickness of the wood veneer has around a 20% decrease during drying ($\frac{h'}{h} = 0.8$). We first discuss the thickness shrinkage effect during dying on the curvature change, as shown in Supplementary Fig. 3. At the dry state, the plastic deformation strain can be expressed as

$$\epsilon_p = (y'_2 - y')\kappa', \tag{6}$$

where $y' = \frac{h'}{h}y$ is the scaled coordinate along the thickness direction, y'_2 is the new boundary of the plastic region, and κ' is an effective curvature. This mapping indicate that the dry configuration can be effectively obtained by molding a flat sheet with thickness of t' under the bending curvature of to κ'. Therefore, the previous analysis in part 1 can be directly leveraged to predict the curvature at the dry state as

$$\frac{\kappa_d}{\kappa\prime} = \left(\frac{1}{2} + 2\left(-\frac{1}{2} + \sqrt{\frac{2\epsilon_{Y_1}}{\kappa' h\prime}}\right)^3 - \frac{3}{2}\left(-\frac{1}{2} + \sqrt{\frac{2\epsilon_{Y_1}}{\kappa' h\prime}}\right)\right). \tag{7}$$

Based on the reversable actuation in multiple dehydration and hydration cycles, we postulate that plastic deformation remains unchanged during the whole transformation process. This leads to a simple relationship between κ' and κ, such that

$$\kappa' h' = \kappa h. \tag{8}$$

Combining Equations (7) and (8), we can have

$$\frac{\kappa_d}{\kappa_w} = \frac{h}{h\prime}. \tag{9}$$

Although our schematic model is focused on the ideal plastic case, it can be shown that the same relationship in Equation (9) also holds for the cases with stiffening.

Equation (9) can account for around 25% increase in the curvature from the wet to the dry state as the thickness decreases is ~ 20%. This is still lower than the experimental observation of the curvature ratio (~2.0 in Fig. 2h). We next examine the gradient length change during drying, which can be attributed to a strain-dependent shrinkage during dehydration and has been reported in previous studies[53,54]. To simplify our analysis, we first decouple this effect with the thickness change and assume the thickness keeps as a constant value. Here, we assume the non-uniform shrinkage is proportional to the mechanical strain at the wet state,

$$\epsilon_w = \epsilon_w^0 - \beta\kappa_w y, \tag{10}$$

where ϵ_w^0 denotes a constant shrinkage, β describs the coupling between the mechanical strain and shrinkage, y is the coordinate along the thickness direction, and $\kappa_w y$ characterizes the mechanical strain distribution. Note we focus on the comparison between the curvatures at the two ending states and neglect the kinetic effects, which deserves more detailed studies in the future. After taking the shrinkage strain, the stress at the dry state σ_d should be modified as

$$\sigma_d = \sigma_w - \epsilon_w E, \tag{11}$$

where σ_w is the stress at the wet state and described in Equations (8) and (15) in Supplementary Note 1. The corresponding equilibrium equations are

$$\int_{-\frac{h}{2}}^{\frac{h}{2}} \sigma_d dy = \int_{-\frac{h}{2}}^{\frac{h}{2}} \sigma_w dy - (E\epsilon_w^0 h) = 0, \tag{12}$$

and

$$\int_{-\frac{h}{2}}^{\frac{h}{2}} \sigma_d y dy = \int_{-\frac{h}{2}}^{\frac{h}{2}} \sigma_w y dy + \frac{1}{12}\beta\kappa_w h^3. \tag{13}$$

It is interesting to note that the non-uniform shrinkage strain only adds one constant term to the existing equations. The dry curvature can be solved from Equation (13) as

$$\frac{\kappa_d}{\kappa} = \frac{\kappa_w}{\kappa}(1+\beta). \tag{14}$$

Now we can directly express the curvature ratio between the dry and wet state as

$$\frac{\kappa_d}{\kappa_w} = 1 + \beta. \tag{15}$$

The same argument of the thickness shrinkage effect can be applied to the dry sample. Therefore, we can further superimpose the thickness shrinkage to the curvature to give a final curvature ratio

$$\frac{\kappa_d}{\kappa_w} = (1+\beta)\frac{h}{h'}. \tag{16}$$

Modeling and simulations. We develop a phenomenological model to simulate the coiling and drilling processes of the seed carrier from inspiration of manufacturing and deployment of the wood-based seed carriers (Supplementary Notes 2-4). The coiling and uncoiling process of wood veneers are modeled as shape morphing of a mechanically anisotropic strip driven by anisotropic contraction and expansion that mimic the effect moisture change (Supplementary Note 2). We next apply the model to representative experimental structures and analyze the thrust force of the coiling body (Supplementary Note 3). The material properties, including elastic moduli and expansion ratios are fitted with experimentally measured coiling geometries and thrust forces, which will be used in the simulations of the drilling process. We finally developed simulation models to study the drilling process of seed carrier with both body and tails (Supplementary Note 4). We show the effects of the tip can be partially explained by prescribing proper boundary conditions. All the simulations are conducted with ABAQUS/Implicit.

References

51. Stamp, N. E. Seed dispersal of four sympatric grassland annual species of Erodium. *J. Ecol.* **77**, 1005 (1989).
52. Yang, N., Li, T. & Zhang, L. A two-dimensional lattice model for simulating the failure and fracture behavior of wood. *Wood Sci. Technol.* **54**, 63–87 (2020).
53. Hanhijärvi, A. Advances in the knowledge of the influence of moisture changes on the long-term mechanical performance of timber structures. *Mater. Struct.* **33**, 43 (2000).
54. Fortino, S., Mirianon, F. & Toratti, T. A 3D moisture-stress FEM analysis for time dependent problems in timber structures. *Mech. Time-Depend. Mater.* **13**, 333 (2009).

Data availability. All data generated and analyzed during the study and the code for generating the coiled body and simulating the drilling process are available upon request. Correspondence and requests for materials, digital models, code and dataset should be addressed to guanyun@zju.edu.cn, shuyang@seas.upenn.edu, tzhang48@syr.edu, liningy@andrew.cmu.edu.

Acknowledgements. We thank Chengyuan Wei, Eran Sharon and Jianzhe Gu for their insightful suggestions. The authors acknowledge funding support from the U.S. National Science Foundation, including IIS-CAREER-1847149 (L.Y.), CMMI-2020476 (T.Z.) and the Future Eco Manufacturing Research Grant (FMRG), # CMMI 2037097 (S.Y.). Simulations were performed

at the Triton Shared Computing Cluster at the San Diego Supercomputer Center and the Expanse cluster (TG-MSS170004, T.Z.) in The Extreme Science and Engineering Discovery Environment. The authors also acknowledge the use of the Materials Characterization Facility at Carnegie Mellon University supported by grant MCF-677785, the National Natural Science Foundation of China (62002321, G.W.), and the gift grant from Accenture Labs.

Author contributions. L.Y. and D.L. conceived the initial concept. A.M. and A.D conceived two application contexts. L.Y., T.Z., S.Y., G.W. and L.S. supervised the project. D.L., L.Y., T.Z. and S.Y. wrote the manuscript. D.L., G.W. and L.Y. performed fabrication and peak force measurements. D.L., L.Y., G.W., J.L., Y.Y. and Y.T. performed drilling tests. D.L. performed bending angle measurement and germination tests. D.L. and L.Y. performed SEM and micrograph analysis. T.Z. and L.Y. performed curvature analysis. T.Z. performed mechanical modeling and simulation. S.Y., T.Z. and L.Y. provided scientific and experimental advice. All authors commented on the manuscript.

Competing interests. There is a provisional patent related to this work filed by Carnegie Mellon University with the U.S. patent office (assignors: L.Y., G.W., J.G., D.L. and F.Q.; application no. 63/173,051 and 63/190,844; currently pending). The other authors declare no competing interests.

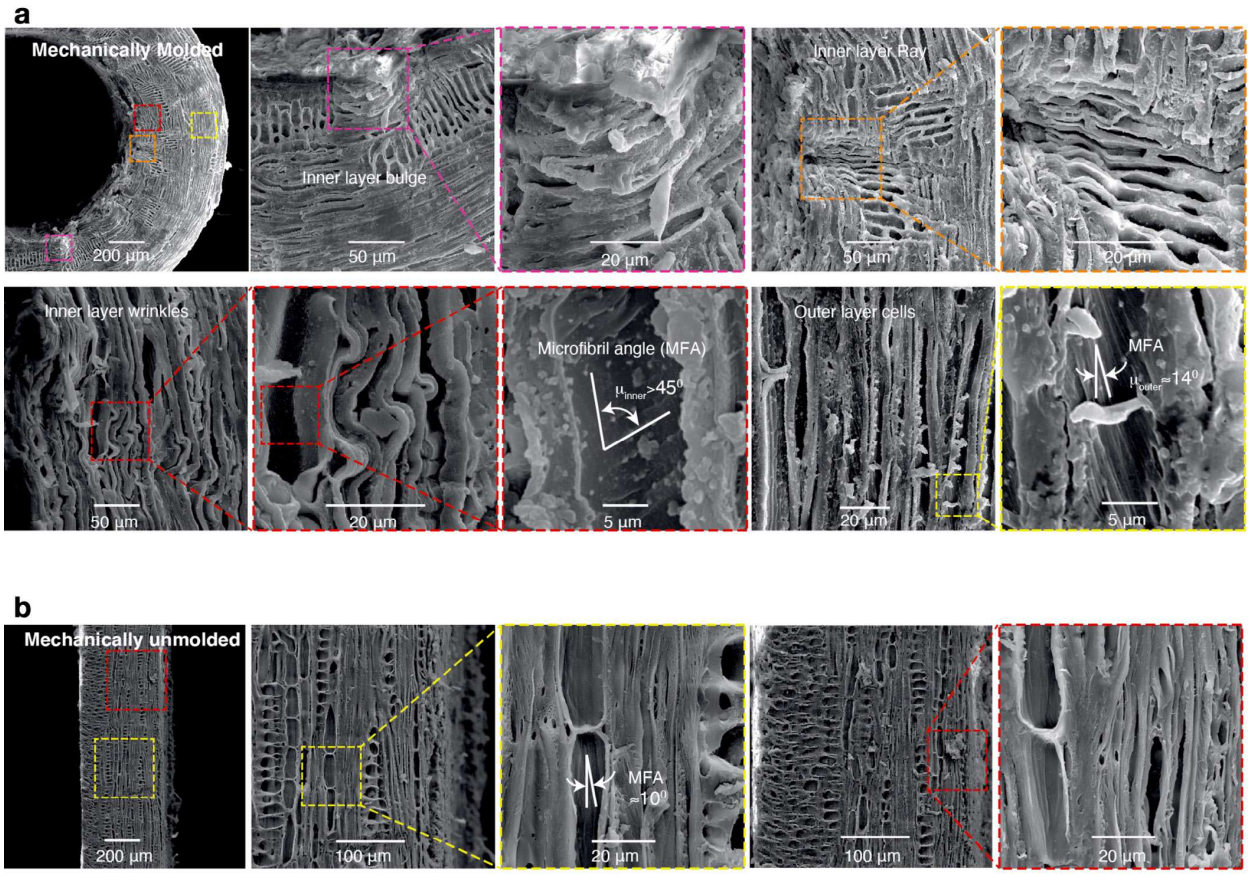

Extended Data Figure 1: SEM images of partially delignified wood veneer. a, Chemically washed and molded wood veneer (0.5 mm thick, 0.8 mm mandrel diameter), showing three different features on the inner side including bulges, compressed rays and wrinkled cell walls that are induced by the mechanical molding and drying. Bulge is caused by mechanical molding on longitudinal cell walls. Medullary rays that are perpendicular to the tree growth direction and parallel to the longitudinal cell walls are a signature of flat sawn white oak. Wrinkled cell walls are also caused by mechanical molding on the longitudinal cells, leading to in-plane deformation of the cell walls. The outer layer cells show no signs of deformation in comparison with (**b**) the chemically washed but not molded wood veneer (0.5 mm thick), showing uniform cell structure throughout the sample.

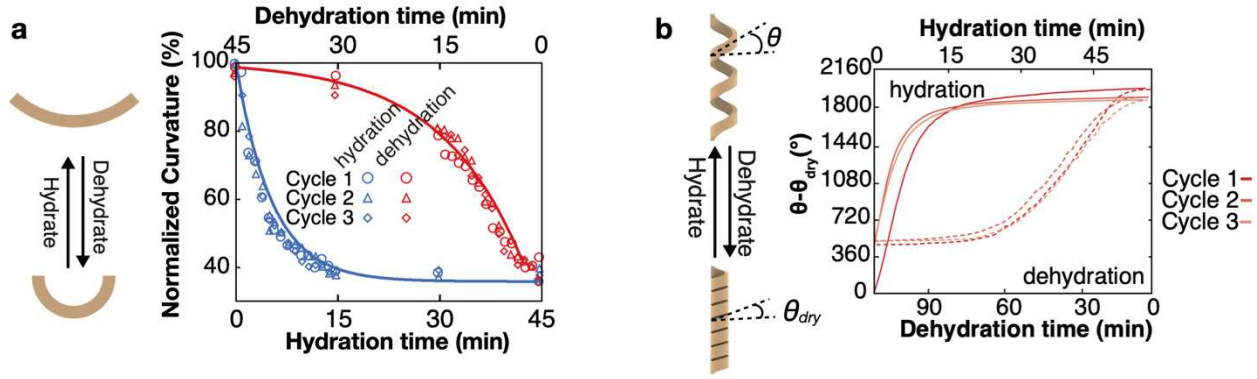

660

661 **Extended Data Figure 2. Performance of the engineered moisture-driven actuators. a,**
662 Reversible curvature changes of a bending actuator during three actuation cycles. **b,** Reversible
663 actuation of a molded coiling actuator in three consecutive hydration-dehydration cycles,
664 showing the angular changes relative to the initial position of the top end of the helix ($\theta - \theta_{dry}$).
665 Both actuators are 3 mm in width and 0.5 mm in thickness, molded with a mandrel with a
666 0.8 mm diameter. The length is 3 mm in (a) and 40 mm in (b).

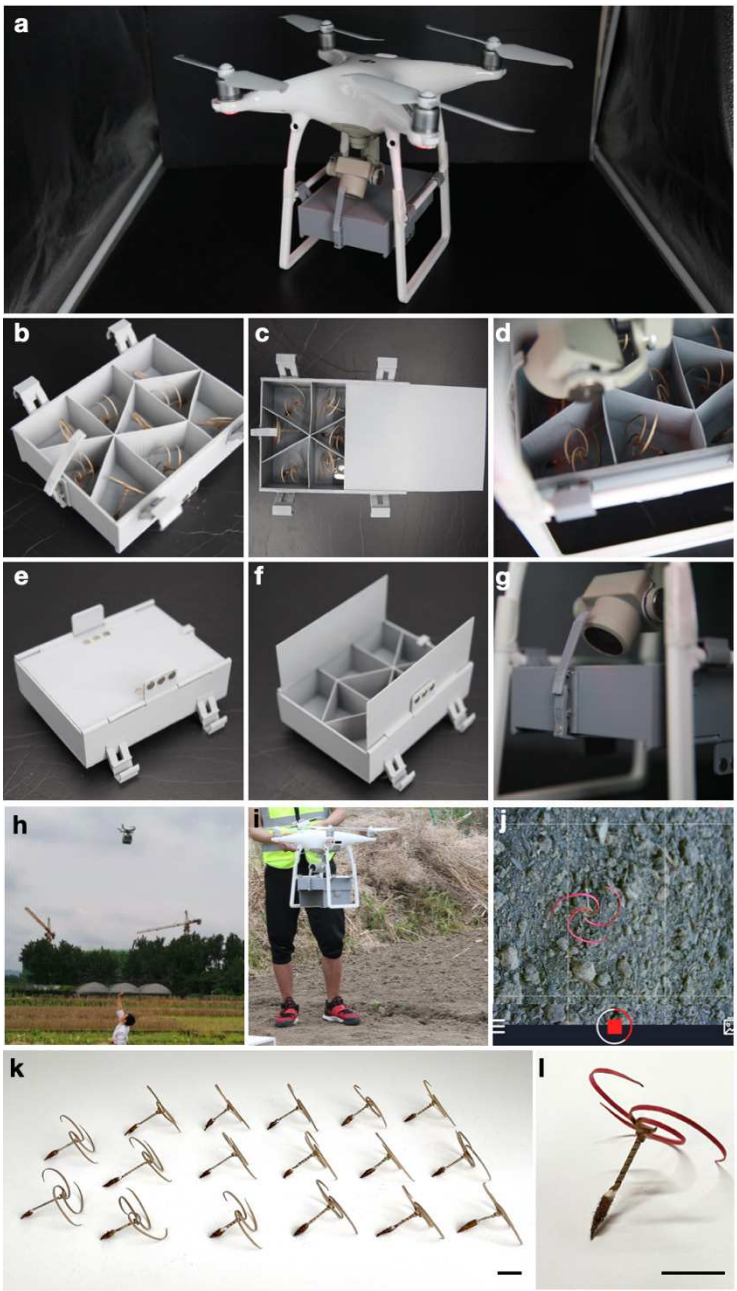

Extended Data Figure 3. Design of a remotely controlled device that can be attached to a drone to carry and deploy seeds. a, Photo of the customized seed deployment mechanism attached to a drone. **b-d,** Top view of the device with a sliding cover to prevent the turbulence caused by the wings of the drone from affecting the deployment. **e-f,** Bottom view of the device, with a magnetic double-side door that can be opened with a remotely controlled pulling mechanism shown in (**g**). **h-j,** A field test of the aerial delivery with examination of the landing pose of the seed carriers. **k-l**, a portion of the seed carriers for the aerial delivery test. The tails are dyed with bright colors for easy identification. Scale bar: 10 mm.

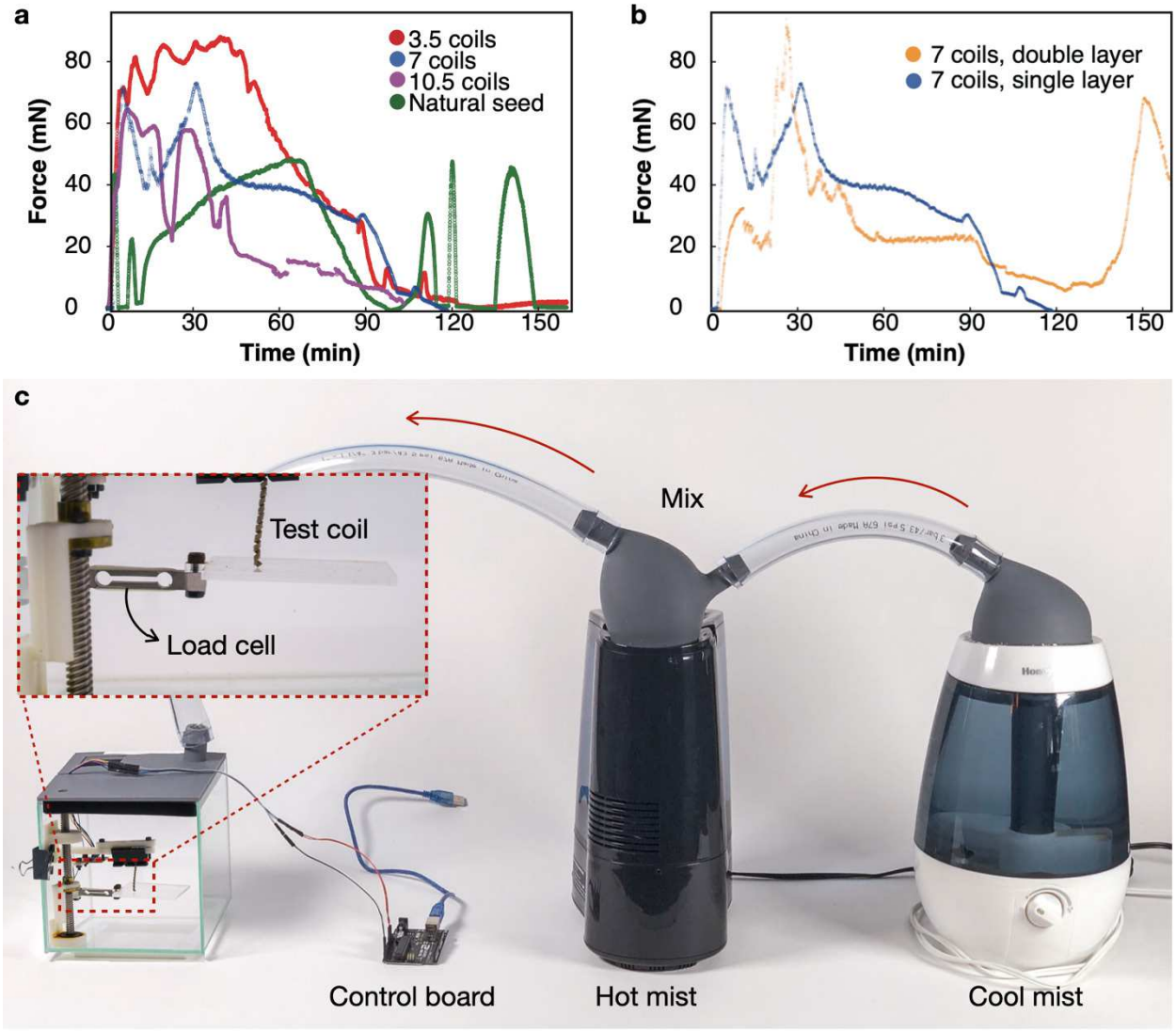

Extended Data Figure 4: Measured extension force. a, Comparison of the engineered coils with different coil numbers with an *Erodium* awn (3.5 body coils). **b**, Comparison of single-coiled and double-coiled actuators with 7 coils in length. **c**, Customized testing setup.

Extended Data Figure 5. Photos of the fabrication and assembly of the seed carrier prototypes. (**a-d**), Processing white oak lumber (**a**) into 0.4 mm thick veneer, through flattening in a planer (**b**), thinning in a band saw (**c**) and surface polishing in a wide belt sander (**d**). **e**, Chemical washing of wood strips. **f-g,** mechanical molding of the washed wood strips beginning from the tail (**f**) molded around a 3D-printed base, and ending with the coiled body (**g**) molded around a mandrel of 0.8 mm in diameter. **h**, The wood veneer is released while it is still wet. **i**, The released wood veneer is gradually tightened until it is fully dried (**j**), resembling the shape of an *Erodium* seed. **k-m**, Fabrication of a three-tailed artificial seed. Two separately molded tails are glued onto the end of the active coil of the original artificial seed. **n-o**, Loading the carrier with two radish seeds covered in flour-based dough. **p**, The two-part tip mold is squeezed to yield the tip shape (**r**) and left for drying for 12 hours. **s**, The dried tip is dipped in 20 wt% ethyl cellulose/ethanol solution for waterproofing and sticking hairs which are electrostatically flocked onto the tip surface (**t**). **u**, A finished three-tailed artificial seed carrier with embedded radish seeds in the tip. For steps **(s-t),** the seed tip fabrication is adapted from literature[23] with additional seeds embedding. Scale bar: 10 mm.

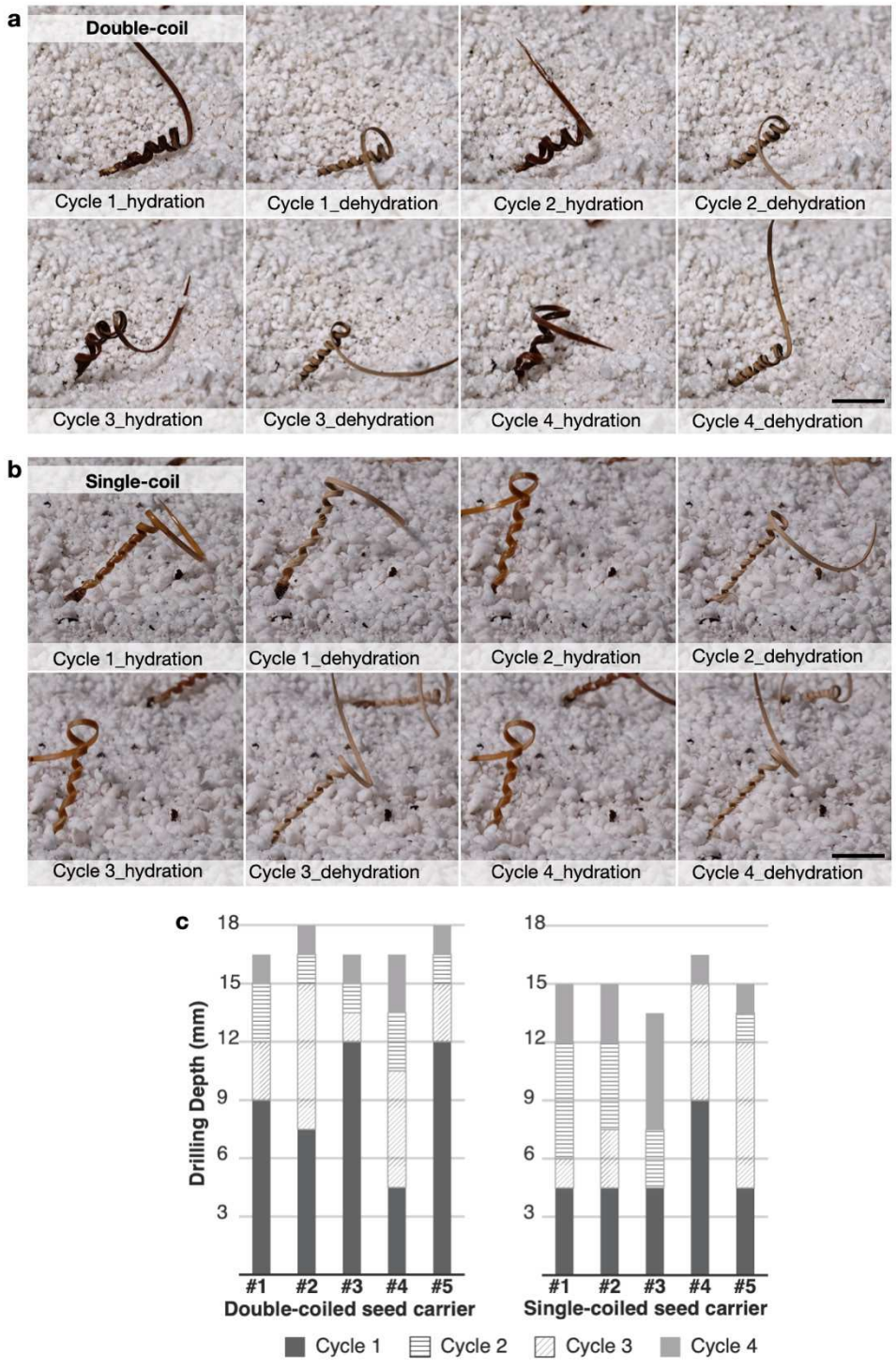

Extended Data Figure 6. Comparison of the self-drilling depth between a double-coiled and a single-coiled seed carrier. a-b, Photos of four cycles of a double-coiled seed carrier (**a**) and a single-coiled seed carrier (**b**) at each hydration and dehydration states. **c**, The drilling depth profiles of five seed carriers with double-coiled body show improvement in each cycle compared with those with single-coiled body. Scale bar: 10 mm.

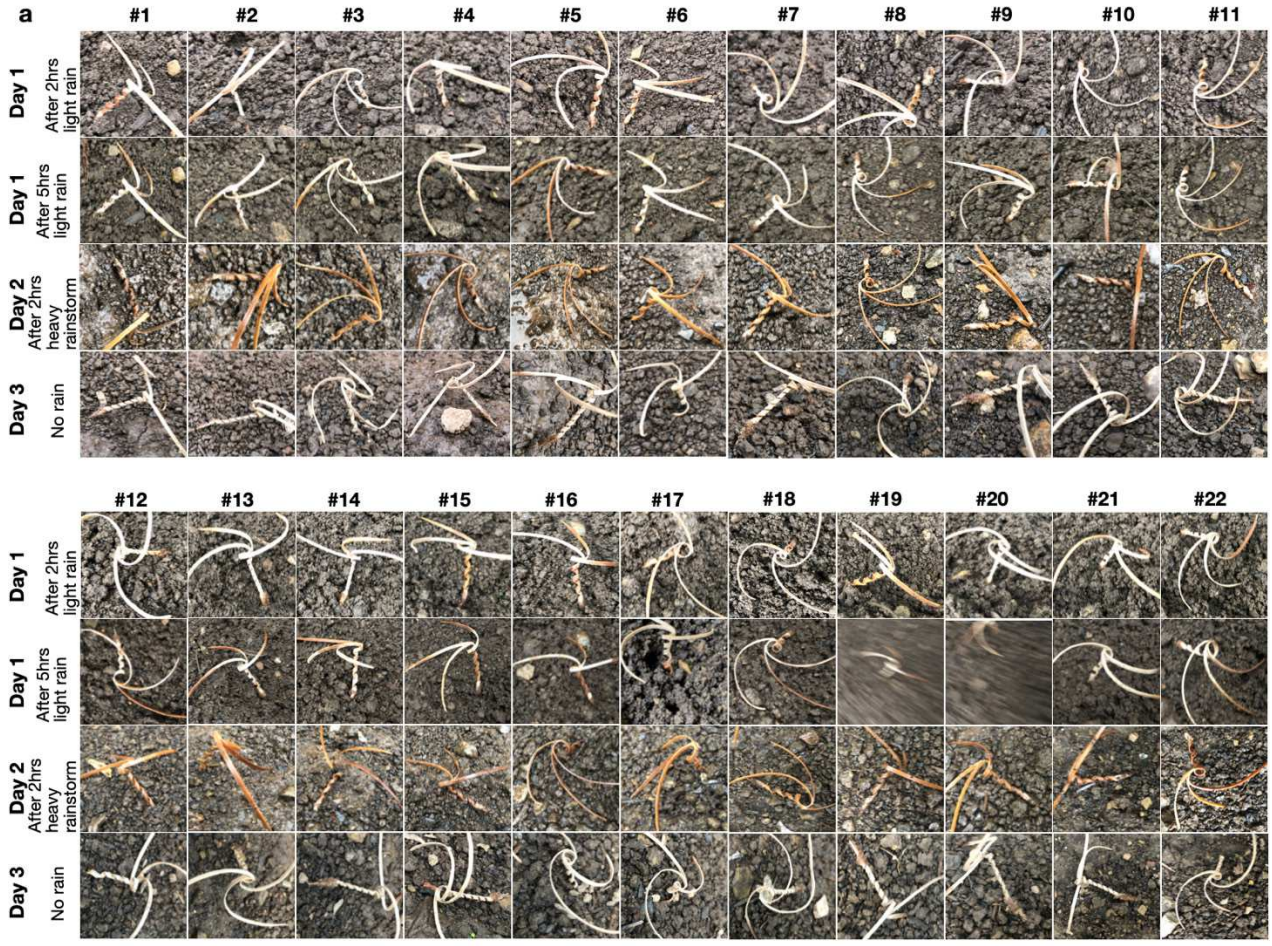

b

	Anchored	Established	Out
Day 1: After 2hrs light rain	15	6	1
Day 2: After 5hrs light rain	11	8	3
Day 2: After 2hrs heavy rain storm	2	6	14
Day 3: No rain	5	6	11

c

Extended Data Figure 7. A field test with 22 three-tailed seed carriers under natural conditions for three consecutive days. a, The drilling progress. **b**, Summary of the drilling performance. **c**, Measurement of the field-testing soil topology.

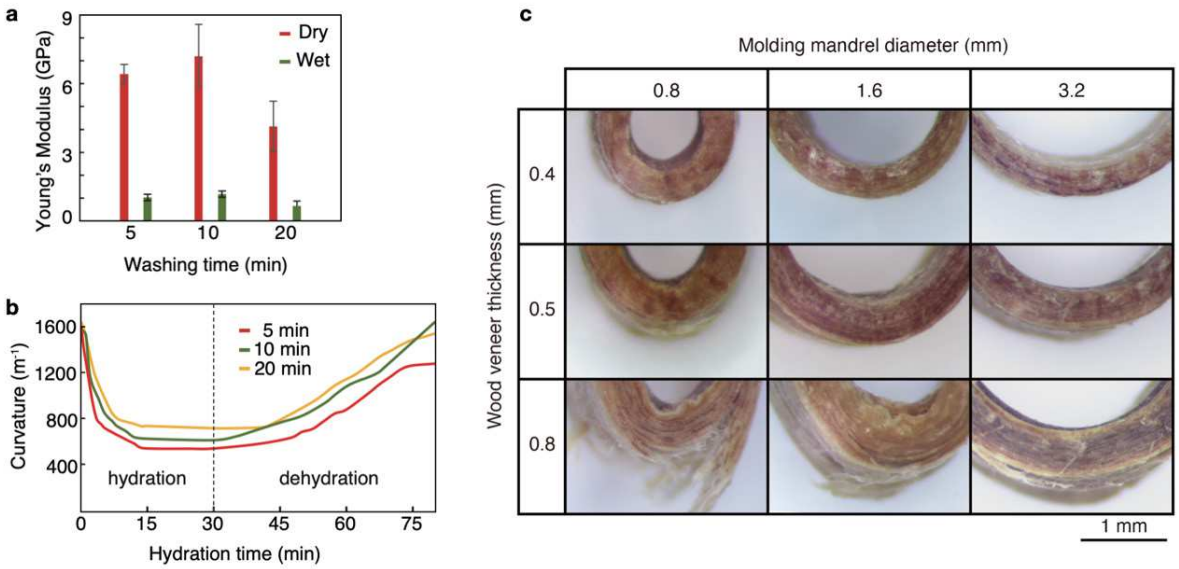

Extended Data Figure 8. Effects of the chemical washing. a-b, Effect of the washing duration on the Young's Modulus (**a**) and curvature changes (**b**). The bending samples for (**a**) and (**b**) are 3 mm in length, 3 mm in width, and 0.5 mm in thickness, molded with a mandrel with a 0.8 mm diameter. **c,** Molding quality comparison on wood veneer of different thickness molded on mandrels with different diameters. The samples for (**c**) are 3 mm in length, 3 mm in width, and 0.5 mm in thickness, with a 10-minute washing duration.

Supplementary Information

This PDF file includes:

Supplementary Table S1 to S3

Supplementary Figures S1 to S9

Supplementary Note S1-S4

Supplementary Videos S1 to S8

Table S1. Comparison of the Young's Modulus, availability/cost and processability for cm scale devices with representative examples of water-responsive materials with promising actuation properties.

Water-responsive Actuating Materials		**Actuation Type**	**Bending Amplitude (m^{-1})**	**Cost/ Availa-bility**	**Young's Modulus (MPa) (RH 20%)**	**Young's Modulus (MPa) (RH 90%)**	**Processability of cm-scale actuators**
Bio-derived Materials	Wood veneer (this work)	Bending & Coiling	480-1854	$	7200	1200	•••
	Wood laminates[15–17]	Bending	0-40	$	14000	-	•••
	Spider silk[27]	Linear	NA	$$$	18000	-	•
	Bacteria spore/cells[28,55]	Bending	0-203	$$$	7000-13000	-	•
	Keratin[42]	Bending & Linear	0-200	$	2000	-	••
	Pollen[56]	Bending	0-220	$$	1460	660	•••
	Pollen-toner[30]	Bending & Coiling	0-800	$$	1460	660	•••
	Starch/flour[57]	Bending & Coiling	0 - 200	$	0.08-0.13		•••
	Gelatin- amyloid (Gel-Am) [58,59]	Coiling	0 - 500	$	0.04 – 0.1	-	••
	β -silk[29]	Bending	800 - 1600	$$	4100-7200	-	•••
	Gelatin biogel[33]	-	-	$	0.02-0.11	-	•••
	Double-crosslinked cellulose[34]	-	-	$$	0.1-5	-	•••
Biological tissues	Pine cone[60]	Bending	-5-58	$	4530	-	••
	Erodium seed awn[25]	Coiling	0-~1000	$	9000	-	••
	Wheat awn[61]	Bending	5-~200	$	10000-20500	-	••
	Chiral seed pod[62]	Coiling	0-~200	$	~15000	-	••
Synthesized Materials	Hygrobot[50] (PEG)	Bending	0-110	$	169	-	•••
	PDMS-PDOT:PSS[63]	Bending	0-350	$$	2	-	•••
	TNF film[64] (TiO_2 nano-capillary)	Bending	0-100	$$	700	-	•••
	PEE-PPy[65] (pentaerythritol ethoxylate-polypyrol)	Bending	-125-125	$	2200	650	•••
	PPy[66] (polypyrol film)	Bending	0-170	$	2500	1650	•••

Table S2: Young's moduli and elastic ratios for various species with approximately 12% moisture content. Adapted from[67].

Wood types	E_L (MPa)	E_T/E_L	E_R/E_L
Hardwood			
Oak, white (chosen in this work)	**13530**	**0.072**	**0.163**
Basswood	11110	0.027	0.066
Birch, yellow	15290	0.050	0.078
Cherry, black	11330	0.086	0.197
Cottonwood, eastern	10340	0.047	0.083
Maple, sugar	13860	0.065	0.132
Walnut, black	12760	0.056	0.106
Softwood			
Baldcypress	10890	0.039	0.084
Cedar, northern white	6050	0.081	0.183
Cedar, western red	8470	0.055	0.081
Douglas-fir – Interior Northern	13530	0.050	0.068
Hemlock, western	12430	0.031	0.058
Larch, western	14190	0.065	0.079
Pine, ponderosa	9790	0.083	0.122
Redwood – Old-grown	10120	0.089	0.087
Spruce, Engelmann	9790	0.059	0.128

Table S3. Material properties of the wood coils

E_1 (GPa)	E_2 (GPa)	E_3 (GPa)	v_{12}	v_{13}	v_{23}	G_{12} (GPa)	G_{13} (GPa)	G_{23} (GPa)	Density $\rho(kg/m^3)$	Dam ping
0.5	0.05	0.05	0.3	0.3	0.3	0.05	0.05	0.05	10^3	0.1
D^d_{coil} (mm)	P^d_{coil} (mm)	Ψ_0 (°)	Ψ_1 (°)	$\epsilon^0_{x'x'}$	$\epsilon^0_{y'y'}$	$\epsilon^0_{z'z'}$	θ_l (°)	θ_{s_x} (°)	θ_{s_z} (°)	t_d (s)
1.82	2.0	60	70	0.1	-0.18	-0.2	20	17.85	14.78	1500

Supplementary Note 1: Curvature in the wet sate just after release

We first analyze the intrinsic curvature (κ_w) for wood veneers within the ideal plastic deformation region. During the molding process (Supplementary Fig. 1a), the deformation strain is

$$\epsilon = (y_1 - y)\kappa, -h/2 < y < h/2\ , \tag{1}$$

where y_1 is the coordinate of the neutral axis, and κ is the bending curvature respect to the neutral axis. The associated stress distribution along the thickness direction can be expressed as (Supplementary Fig. 1b, c)

$$\sigma = (y_1 - y)\kappa E,\ y < y_2 \text{ and } \sigma = -\sigma_Y,\ y > y_2, \tag{2}$$

where E is the Young's modulus along longitude direction, σ_Y is the absolute value of the plastic yielding stress, and y_2 is the boundary between the elastically and plastically deformed regions. The governing equations include the stress continuity at y_2 and the stress equilibrium equation, such that

$$(y_1 - y_2)\kappa E = -\sigma_Y \text{ and } \int_{-\frac{h}{2}}^{\frac{h}{2}} \sigma dy = 0. \tag{3}$$

Solving Equation (3) gives

$$y_1 = -\frac{h}{2} + \sqrt{\frac{2\epsilon_{Y_1} h}{\kappa}} - \frac{\epsilon_{Y_1}}{\kappa} \text{ and } y_2 = -\frac{h}{2} + \sqrt{\frac{2\epsilon_{Y_1} h}{\kappa}}. \tag{4}$$

We next apply the condition $\frac{1}{\kappa} - \left(\frac{h}{2} - y_1\right) = R$ and solve the unknow curvature κ as

$$\kappa = \frac{4\left(1-\epsilon_{Y_1}\right)^2}{\left(\sqrt{2\epsilon_{Y_1} h + 4(R+h)\left(1-\epsilon_{Y_1}\right)} - \sqrt{2\epsilon_{Y_1} h}\right)^2}\ . \tag{5}$$

The plastic deformation strain in the inner part is

$$\epsilon_p = (y_2 - y)\kappa, y > y_2. \quad (6)$$

After released from the mold, the elastic part tends to recover to the flat state while the plastically deformed part prefers to remain in the deformed configuration, which leads to an unknown intrinsic curvature κ_w (Supplementary Fig. 1d). The deformation strain at the released state is

$$\epsilon = (y_3 - y)\kappa_w, \quad (7)$$

where y_3 is a new neutral axis and unknown variable. The stress distribution in the released sample can be expressed as

$$\sigma = (y_3 - y)\kappa_w E,\ y < y_2, \text{ and } \sigma = \big((y_3 - y)\kappa_w - (y_2 - y)\kappa\big)E, y > y_2. \quad (8)$$

Since the wood veneer is in self-equilibrium, we have the following stress and moment equilibrium equations

$$\int_{-\frac{h}{2}}^{\frac{h}{2}} \sigma dy = 0, \quad (9a)$$

We can obtain κ_w from Equations (8) and (9a)

$$\int_{-\frac{h}{2}}^{\frac{h}{2}} \sigma y dy = 0. \quad (9b)$$

We can obtain κ_w from Equations (9a-b)

$$\frac{\kappa_w}{\kappa} = \left(\frac{1}{2} + 2\left(-\frac{1}{2} + \sqrt{\frac{2\epsilon_{Y_1}}{\kappa h}}\right)^3 - \frac{3}{2}\left(-\frac{1}{2} + \sqrt{\frac{2\epsilon_{Y_1}}{\kappa h}}\right)\right). \quad (10)$$

Equation (10) shows that wood veneers with different thickness and mold curvatures will follow a master curve, which is validated by our experimental data (Fig. 2g).

We next apply the same analysis to wood veneers within the stiffening deformation region. Although the deformation stain formula remains the same, we need to rewrite the stress during the molding (Supplementary Fig. 2b, c) as

$$\sigma = \{(y_1 - y)\kappa E,\ y < y_2\ -\sigma_Y,\ y_2 < y < y_4\ -\sigma_Y + \left((y_1 - y)\kappa + \epsilon_{Y_2}\right)E,\ y > y_4\ , \tag{11}$$

where ϵ_{Y_2} is the critical strain for stiffening and $y_4 = y_1 + \epsilon_{Y_2}/\kappa$ denotes the boundary of the densification region. Substituting the stress into the same governing equation (Equation (3)), we can obtain

$$\kappa = \frac{\frac{R}{h}(\epsilon_{Y_2} - \epsilon_{Y_1}) + 1 \sqrt{\left(\frac{R}{h}(\epsilon_{Y_2} - \epsilon_{Y_1}) + 1\right)^2 - 4\left(\frac{R}{h} + \frac{1}{2}\right)\left((\epsilon_{Y_2} - \epsilon_{Y_1}) - \frac{1}{2}\left(\epsilon_{Y_2}^2 - \epsilon_{Y_1}^2\right)\right)}}{2R + h}, \tag{12}$$

and

$$y_1 = \left(\kappa h + \epsilon_{Y_1} - \epsilon_{Y_2}\right)^{-1}\left(\frac{1}{2\kappa}\left(\epsilon_{Y_2}^2 - \epsilon_{Y_1}^2\right) - \frac{h}{2}\left(\epsilon_{Y_2} - \epsilon_{Y_1}\right)\right), \tag{13}$$

The plastic deformation strain in the wood veneer is

$$\epsilon_p = \{0,\ y < y_2\ (y_2 - y)\kappa,\ y_2 < y < y_4\ \epsilon_{Y_1} - \epsilon_{Y_2},\ y > y_4\ . \tag{14}$$

After released from the mold, the stress distribution in the released sample can be expressed as

$$\sigma = \{(y_3 - y)\kappa_w E,\ y < y_2\ \left((y_3 - y)\kappa_w - (y_2 - y)\kappa\right)E,\ y_2 < y < y_4\ \left((y_3 - y)\kappa_w + \epsilon_{Y_2} - \epsilon_{Y_1}\right)E,\ y > y_4\ . \tag{15}$$

The same stress and moment equilibrium equations (Equation (9a-b)) still hold for this case, from which we can obtain κ_w as

$$\frac{\kappa_w}{\kappa} = 3\frac{(\epsilon_{Y_2} - \epsilon_{Y_1})}{\kappa h}\left(1 - 4\left(\frac{y_4}{h}\right)^2\right) + \left(4\left(\frac{y_4}{h}\right)^3 + 2\left(\frac{y_2}{h}\right)^3 - 6\frac{y_2}{h}\left(\frac{y_4}{h}\right)^2\right), \tag{16}$$

where $\frac{y_2}{h} = \frac{y_1}{h} + \frac{\epsilon_{Y_1}}{\kappa h}$ and $\frac{y_4}{h} = \frac{y_1}{h} + \frac{\epsilon_{Y_2}}{\kappa h}$ and y_1 is given by Equation (13).

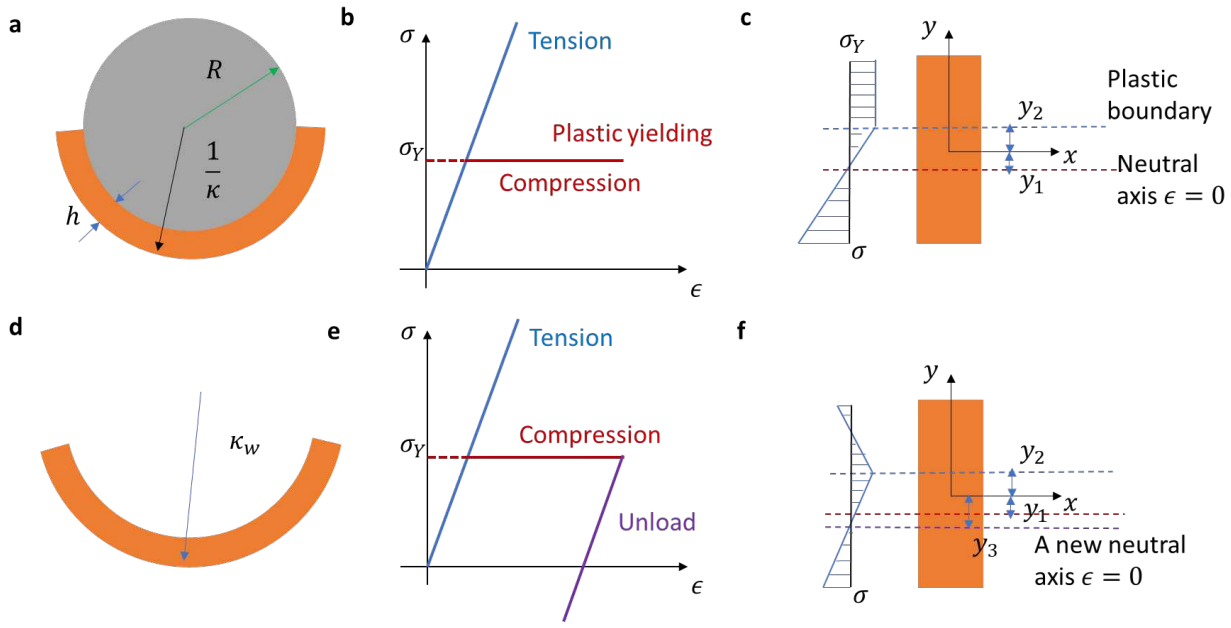

Figure S1. Intrinsic curvatures after release of the wood veneer from the mold within the ideal plastic region. **a**, Molding the chemically washed wood veneer with a thickness t on a mandrel with a radius R. **b**, Plastic stress-strain relations during loading. **c**, The stress distribution along the thickness direction. **d**, Released configuration. **e**, Plastic stress-strain relations during unloading. **f**, The stress distribution in the released sample.

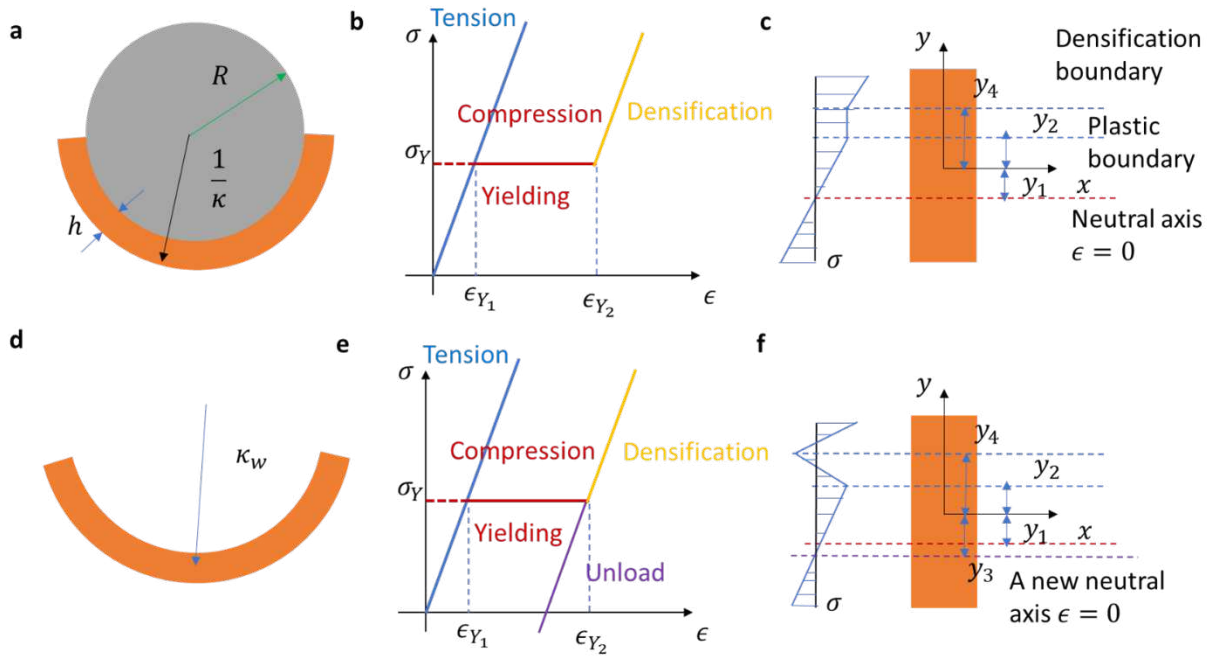

Figure S2. Intrinsic curvatures after release of the wood veneer from the mold within the stiffening region a, Molding. **b**, Plastic stress-strain relations during loading. **c**, The stress distribution along the thickness direction. **d**, Released configuration. **e**, Plastic stress-strain relations during unloading. **f**, The stress distribution in the released sample.

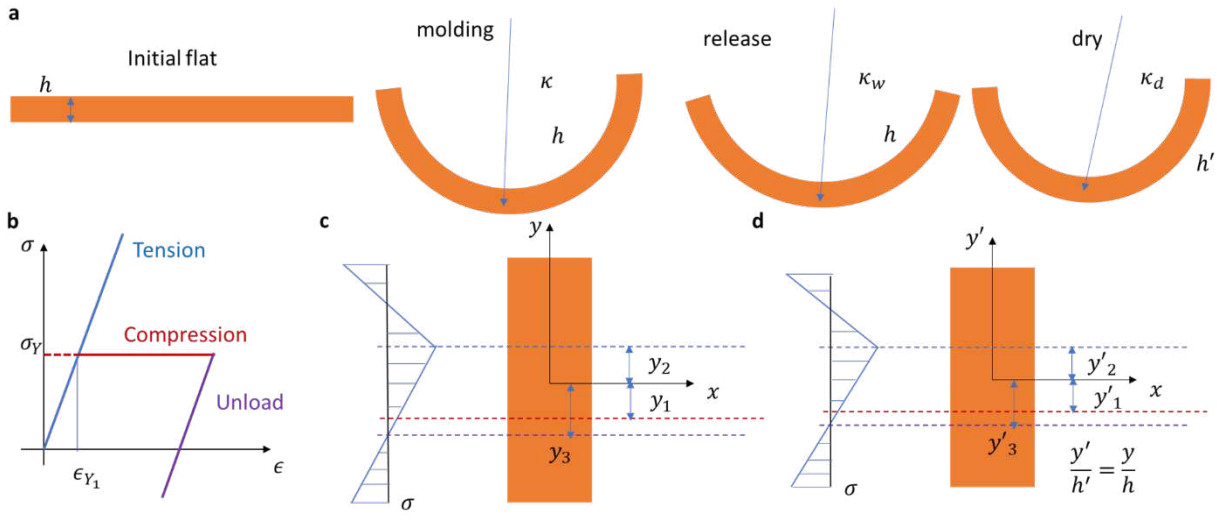

Figure S3. **The thickness shrinkage effect during drying on the curvature change**. **a**, The manufacturing processes. **b**, Plastic model. **c**, The stress distribution at the wet state. **d**, The stress distribution at the dry state.

Supplementary Note 2: A theoretical model of the wood coils.

We develop a phenomenological model to simulate the coiling and drilling processes of the seed carrier from inspiration of manufacturing and deployment of the wood-based seed carriers. It is noted that we do not intend to capture the detailed structure-property relationship of the wood materials but to predict the shapes and forces of the wood coils by tuning the elastic constants and hydration strain to match the experimental data. Although the model is much more simplified than the real structures, we find good agreements between simulation and experiments, and uncover the key design principles for enhancing drilling forces to improve the success rate of seeding.

To form a helix from an initially straight wood strip, we introduce a hydration strain field to the strip, whose principal direction has an inclined angle with the longitudinal center line of the strip. In the simulation, the wood is anisotropic both in mechanical and hydration properties, which are defined in the local coordinate $(x', \mathrm{y}', \mathrm{z}')$. Here, the local longitudinal direction x' represents the direction with maximum stiffness and hydration strain and is defined by a rotation angle θ_l with respect to the globally horizontal direction (x). The anisotropic moduli are defined by engineering constants, including three moduli E_1, E_2, E_3; Poisson's ratios v_{12}, v_{13}, v_{23}; and shear moduli G_{12}, G_{13}, G_{23} which are associated with the material's principal directions. Here the direction 1,2, and 3 corresponds to x', y', and z', respectively. These material parameters define the elastic compliance as

$$\begin{Bmatrix} \epsilon_{11} \\ \epsilon_{22} \\ \epsilon_{33} \\ \gamma_{12} \\ \gamma_{13} \\ \gamma_{23} \end{Bmatrix} = \begin{bmatrix} 1/E_1 & -v_{21}/E_2 & -v_{31}/E_3 & 0 & 0 & 0 \\ -v_{12}/E_1 & 1/E_2 & -v_{32}/E_3 & 0 & 0 & 0 \\ -v_{13}/E_1 & -v_{23}/E_2 & 1/E_3 & 0 & 0 & 0 \\ 0 & 0 & 0 & 1/G_{12} & 0 & 0 \\ 0 & 0 & 0 & 0 & 1/G_{13} & 0 \\ 0 & 0 & 0 & 0 & 0 & 1/G_{23} \end{bmatrix} \begin{Bmatrix} \sigma_{11} \\ \sigma_{22} \\ \sigma_{33} \\ \sigma_{12} \\ \sigma_{13} \\ \sigma_{23} \end{Bmatrix}, \quad (17)$$

where v_{ij} has the physical interpretation of the Poisson's ratio that characterizes the transverse strain in the j-direction, when the material is stressed in the i-direction. In general, v_{ij} and v_{ji} are related by $v_{ij}/E_i = v_{ji}/E_j$.

The hydration strains are generated by virtually rolling the wood strip with respective to a given axis (l') to form a helix with the same diameter and pitch of the dry coil in the experiments

(Supplementary Fig.4). To provide more freedom of fitting the helix diameter and pitch in experiments, we treat the angle of the local longitudinal direction (θ_l), the angle of the effective rolling axis (Ψ) and bending curvature of the coil (κ_{coil}) as fitting parameters in the simulations. The corresponding active hydration strain field[68] can then be defined as

$$\epsilon^{h}_{x'x'} = (z' - h)\kappa_{\mathrm{coil}} \sin^2 \Psi + \epsilon^{\mathrm{a}}_{x'x'},$$

$$\epsilon^{h}_{y'y'} = (z' - h)\kappa_{\mathrm{coil}} \cos^2 \Psi + \epsilon^{a}_{y'y'}, \tag{18}$$

$$\epsilon^{h}_{x'y'} = -(z' - h/2)\kappa_{\mathrm{coil}} \sin \Psi \cos \Psi,$$

where $\epsilon^{u}_{x'x'}$ and $\epsilon^{u}_{y'y'}$ are uniform hydration strain components and $0 \le z' \le h$. In addition, there is a contraction along the thickness, which is assumed uniform and denoted as $\epsilon^{h}_{z'z'}$. The final configuration of the coil will be obtained through mechanical equilibrium under an inputted hydration strain field, defined in Eq. (18).

To effectively represent the hydration state, we introduce a variable ξ ($0 \le \xi \le 1$) to control the shape morphing from a straight strip to a tightly packed dry coil. To simplify the model, we assume the κ_{coil}, Ψ, $\epsilon^{u}_{x'x'}$, $\epsilon^{u}_{y'y'}$, and $\epsilon^{h}_{z'z'}$ are linear functions of ξ, with $\xi = 1$ denoting the dry state and $\xi = 0$ corresponding to the initially straight state. Therefore, curvature (κ_{coil}) and rolling axis angle (Ψ) can be defined by

$$\kappa_{\mathrm{coil}}(\xi) = \frac{2D^{d}_{\mathrm{coil}}}{\left(D^{d}_{\mathrm{coil}}\right)^2 + \left(P^{d}_{coil}/\pi\right)^2}\xi, \tag{19}$$

$$\Psi = \Psi_0 + (\Psi_1 - \Psi_0)\xi, \tag{20}$$

$$\epsilon^{u}_{x'x'} = \epsilon^{0}_{x'x'}\xi, \epsilon^{u}_{y'y'} = \epsilon^{0}_{y'y'}\xi, \text{ and } \epsilon^{h}_{z'z'} = \epsilon^{0}_{z'z'}\xi, \tag{21}$$

where D^{d}_{coil} and P^{d}_{coil} are diameter and pitch of the dry coil, Ψ_0 and Ψ_1 are two fitting parameters, $\epsilon^{0}_{x'x'}$, $\epsilon^{0}_{y'y'}$, and $\epsilon^{0}_{z'z'}$ represent the slope of uniform hydration strain components. The wet coil is modeled as the configuration from a non-zero ξ ($\xi = \xi^{w}$), which is determined by the diameter

($D_{\mathrm{coil}}^{\mathrm{w}}$) and pitch (P_{coil}^{w}) in experiments. The dynamical hydration and dehydration processes are described by prescribing a time dependent sequence of ξ.

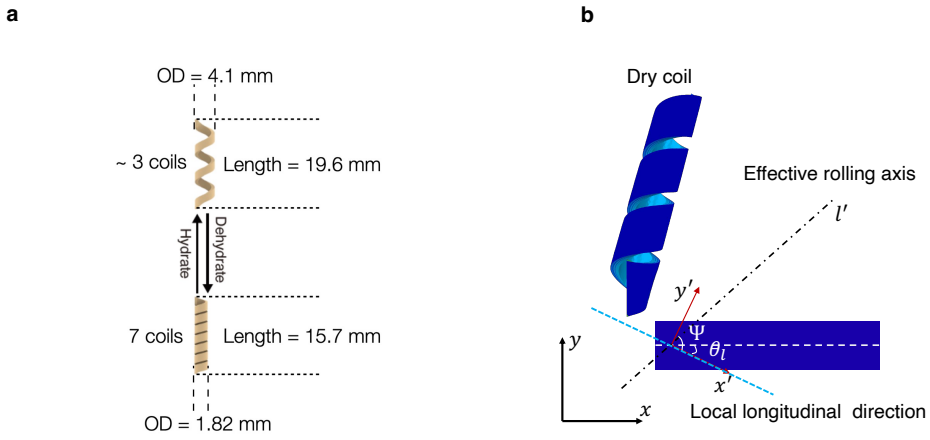

Figure S4. Development of the simulation model for the engineered seed coil. a, Schematic of the experimental seed coils at wet and dry states. **b**, Simulated coils from the straight sheets. The local coordinate $(x', \mathrm{y}', \mathrm{z}')$ is defined by a rotation (θ_l) from the global coordinate $(x, \mathrm{y}, \mathrm{z})$ with respect to z axis. The rolling axis l' has an inclined angle Ψ with x'.

Supplementary Note 3: Simulations of the thrust forces.

We next apply the model to representative experimental structures, as shown in Supplementary Fig.5. In simulations, the initial wood sheet has a thickness (h) of 0.5 mm, and width (b) of 2.5 mm. Three different lengths (including 25 mm, 48 mm, and 75 mm) are chosen, which correspond to 3.5 coils, 7 coils, and 10 coils, respectively. The material properties of the wood materials are listed in Supplementary Table S3. Note that these parameters are fitted by comparing the simulations with experiments and are generally not unique. However, we do not expect the non-uniqueness of the material parameters will qualitatively change the conclusions. The model is highly nonlinear, therefore we perform finite element simulations with ABAQUS/implicit to numerically solve the problems. We discretize the structure with 3D wedge elements (C3D6). We create 5 elements along the thickness direction to capture the gradient of the hydration strain and the large bending curvature. Each layer of the elements is assigned with a different hydration strain. The mesh size on the wood plane is set to be 0.25 mm. Moderate dissipation is adopted to help the convergence of the simulations.

The wood sheet has a length of L, width of W, and thickness of h. Before deformation, the wood sheet is rotated $\theta_{S_x}$and θ_{S_z}, with respect to x and z axis, respectively. A local coordinate system is introduced to describe the anisotropy of wood sheet with the local longitudinal direction as x'. The wet and dry coils are described by their diameters (D_{coil}^{w} and D_{coil}^{d}) and pitches (P_{coil}^{w} and P_{coil}^{d}). The color represents the maximum principal deformation strain.

In simulation, we first gradually increase the hydration state variable ξ from 0 to ξ^w to form the initial coil at the wet state and then continue to increase ξ to 1 to form the dry coil. To reproduce the thrust force measurement, we need to generate a vertically aligned coil at the dry state, which can be achieved by rotating the straight strip along the x and z axis (Supplementary Fig.5). The rotation angles θ_{S_x} and θ_{S_z} are first identified from numerical simulations. During the first coiling process, we set the hydration state variable to follow a slow linear ramp from 0 to 1. This is a simplified setting for a quasistatic process. After the coil reaches the dry state, a rigid plate is moved to the coil tip to constrain the coil. We then decrease ξ from 1 to ξ^w following an exponential decay to simulate the force measurement during uncoiling process, such that

$$\xi = \xi^w + (1 - \xi^w)\exp\left(-\frac{t}{t_d}\right), \tag{22}$$

where t_d is a characteristic time scale and can be attributed to the moisture diffusion process. The exponential decay is also observed in our experiments (Fig. 3f). Note that t_d depends on both the material properties and environment conditions. We treat t_d as a fitting parameter to match the time variation of the measured forces in the experiments. We find $t_d = 1500\ s$ can lead to a good agreement with the humidity chamber experiments.

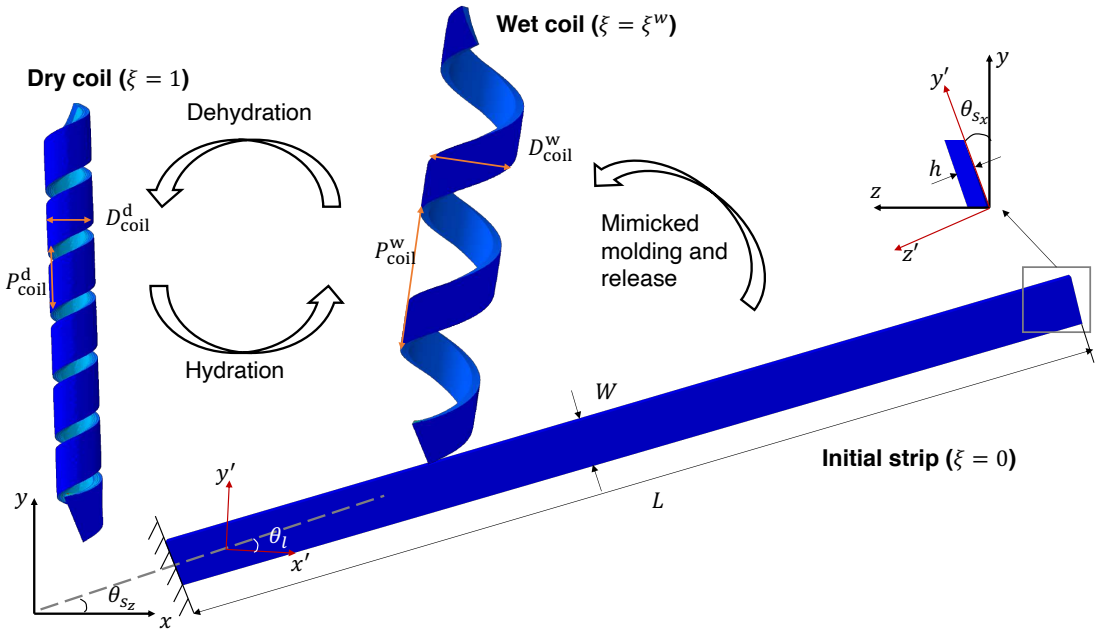

Figure S5. A schematic of the modeling process of the formation and actuation of wood coils. The wood sheet has a length of L, width of W, and thickness of h. Before deformation, the wood sheet is placed at a position of θ_{S_x} and θ_{S_z}, with respect to x and z axis, respectively. A local coordinate system is introduced to quantify the anisotropy of the wood sheet with the local longitudinal direction as x'. The wet and dry coils are described by their diameters (D^w_{coil} and D^d_{coil}) and pitches (P^w_{coil} and P^d_{coil}). The color represents the maximum principal deformation strain.

Supplementary Note 4:

Simulations of the drilling process. We develop simulation models to study the drilling process of seed carrier with both body and tails. Here we do not explicitly include the seed tip because it will make the model too complex to converge. Further, we show the effects of the tip can be partially explained by prescribing proper boundary conditions. We describe the model and simulation setups step by step in the following section.

We first describe the simulation setting for incorporating three tails into the finite element simulations. The single-tail structure is a subset of the three-tail structure; therefore, we can follow the same process and only add the first tail. In the simulation, the tails are glued to the coil body through the "Tie" command in ABAQUS, inspired by the experimental procedure. The initial modeling setups were applied to the initially flat configuration ($\xi = 0$). As shown in Supplementary Fig.6a, the first tail shares the same surface of the body while a narrow region (i.e., 0.5 mm long) of the second and third tails are attached to the top surface of the body. The locations of the bonding sites are chosen to reproduce the tail configurations in our experiments (Fig. 3d). Our experiments show the tails usually does not deform much. This motivates us to choose a simple bilayer model to describe the shape of the tail with one passive layer and one active layer responsive to the moisture change. To keep the model simple, we set the same mechanical properties of tails as the coil body with the only difference of the local longitudinal direction. For the three tails, the local longitudinal directions are given by $(\theta_l)_1 = 0^{\mathrm{o}}$, $(\theta_l)_2 = -5^{\mathrm{o}}$, $(\theta_l)_3 = -10^{\mathrm{o}}$, which are fitting parameters to better match with the experimental configuration.

$$\left(\epsilon^h_{x'x'}\right)_{tail} = -0.025\xi, \left(\epsilon^h_{y'y'}\right)_{tail} = -0.2\xi, \text{ and } \left(\epsilon^h_{z'z'}\right)_{tail} = -0.2\xi. \tag{23}$$

The corresponding configurations for wet and dry coils with tails are given in Supplementary Fig.6 b and c, respectively. Since the simulations do not explicitly model the coil tip, we do not follow the exact same length of the tails. Instead, we choose the tail lengths to make the inclined angle between the three-tail structure and the ground (Supplementary Fig.6d) in simulation match with experimental observations. All the three tails have the same width (2.5 mm) and thickness (0.5 mm) as the coil body. Configurations with one to three tails at the dry states are given in Supplementary Fig.7, from which the bonding sites can be clearly observed.

To numerically model the drilling process, we develop a three-step simulation (Supplementary Fig.8). Since the detailed tail label is not critical information, we set the tail color as yellow as well in the following discussion. In the first step, the body and tails of the coil are formed from an initially straight strip driven by hydration strain. During this step, the bottom surface of the coil body is fixed. In the second step, we release the bottom surface of the coil body to let the coiling system fall under gravity. In the third step, we simulate the drilling motion during hydration.

The interactions between the coiling system (body and tails) and ground are described by frictional contact in ABAQUS. The friction is implemented through the penalty method. We set the friction coefficient between the coil and ground to 0.8. The contact interaction is also stabilized by a small damping factor (0.0001 for automatic stabilization and tangent fraction in the contact control setting in ABAQUS) to overcome the convergence issue. In the simulation, we fully constrain the deformation of ground, which is a much simplified condition. We indeed observe that tail end and seed carrier tip can penetrate the soil surface in our experiments and serve as anchoring points to enhance the drilling forces (Fig. 3d). To mimic the anchoring points, we set the frictional coefficient of the tail ends (purple regions) as 2.0 larger than the tail body (yellow region) in Supplementary Fig.9. Since we do not explicit model the seed carrier tip, we cannot model the anchoring effect by simply adjusting the friction coefficient near the coil end. Here we choose one corner point of the coil body (point A in Supplementary Fig.9) and constrain its motion on the ground (along x and z directions) to mimic the anchoring of the seed carrier tip. We further define a coil end region (highlighted in green in Supplementary Fig.9) to facilitate the calculation the interaction forces between the coil and the ground. The friction coefficient between the coil end and the ground remains as 0.8 because the anchoring effect is described by the displacement constraint of point A. The force applied to the coil end will be the superposition of the contact forces between the coil end and the ground and the reaction forces at point A. A similar setup is applied to the 1-tail structure as well. To compare the seed tip anchoring effects, we also simulate the case without constraining point A. It should be noted that both scenarios are observed in experiments. And our experiments show that the case without tip anchoring is more difficult to establish drilling success than the one with tip anchoring (Supplementary Video S4), which is consistent with the force levels found in simulations.

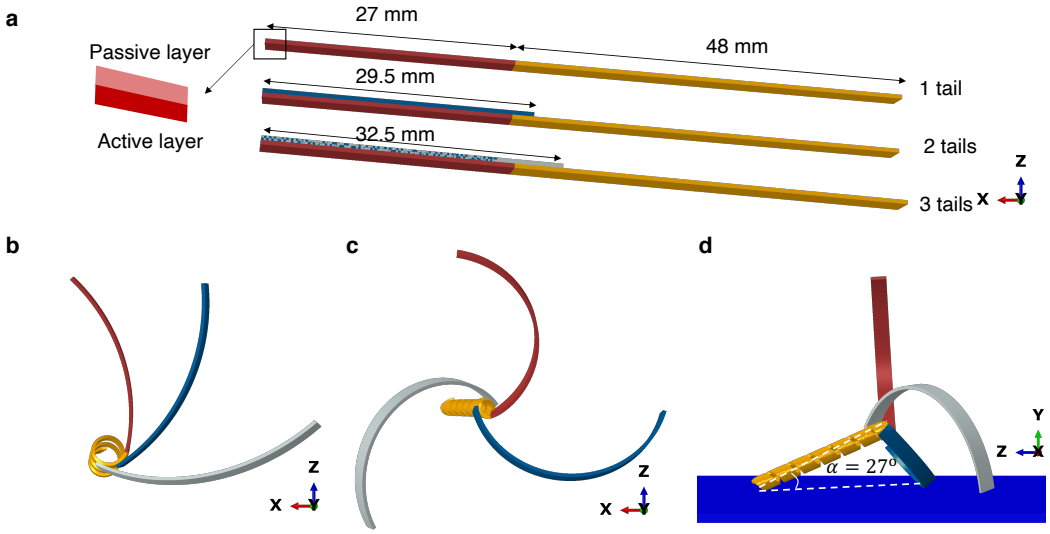

Figure S6. Modeling setup of the coil body and tails. (a) The initial configuration at $\xi = 0$. (b) The configuration at $\xi = 0.45$. (c) The configuration at $\xi = 1$. (d) Simulated three-tailed coil resting on the ground.

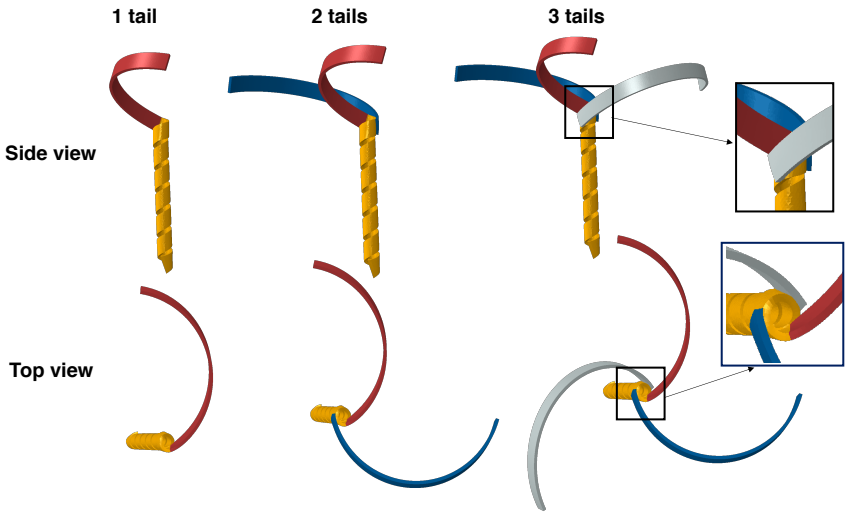

Figure S7. The dry seed coil body with different configurations of tails.

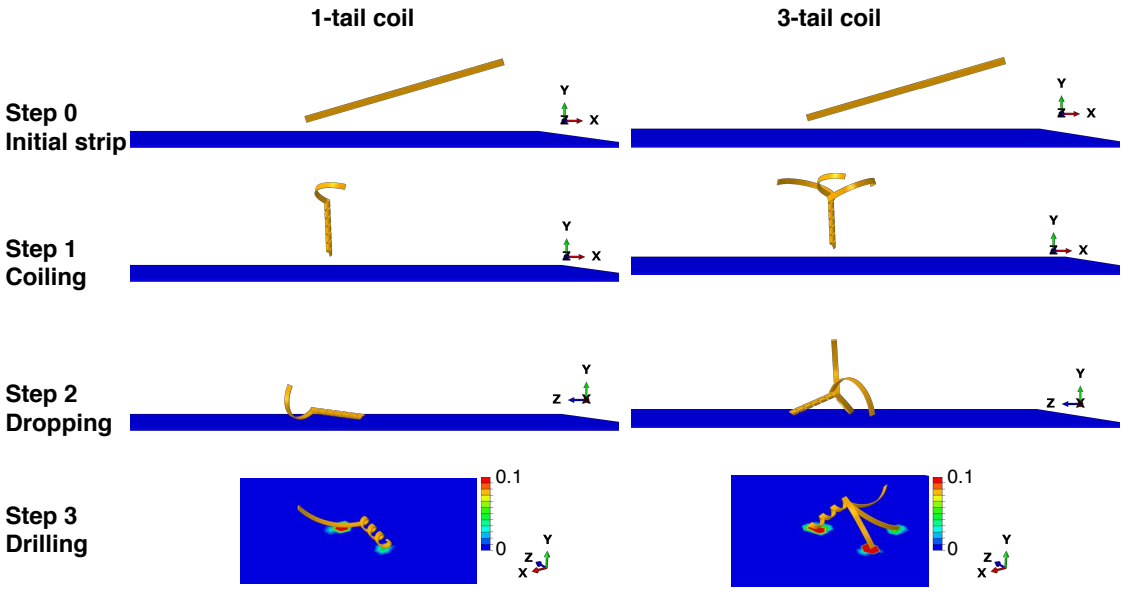

965

966 **Figure S8. The 3-step simulations of the coil drilling process.** The color represents the contact
967 pressure (unit kPa). Note that the maximum contact pressure is larger than 0.1. The choice of the
968 current color bar is to help with the visualization of the contact regions.

969

970

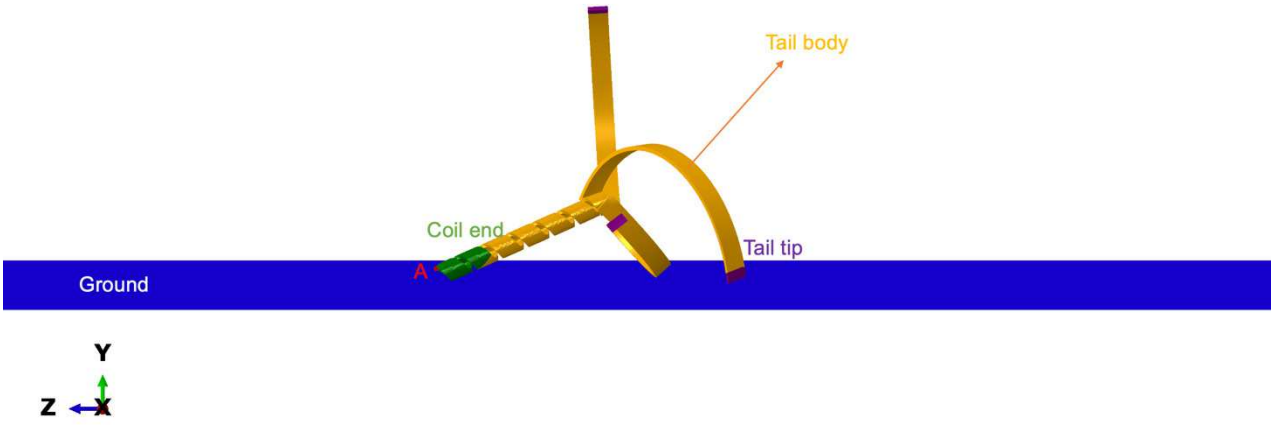

971

972 **Figure S9. Interaction between the coil system and ground.**

References

55. Wang, W. *et al.* Harnessing the hygroscopic and biofluorescent behaviors of genetically tractable microbial cells to design biohybrid wearables. *Sci. Adv.* **3**, e1601984–e1601984 (2017).
56. Zhao, Z. *et al.* Actuation and locomotion driven by moisture in paper made with natural pollen. *Proc. Natl. Acad. Sci.* **117**, 8711–8718 (2020).
57. Tao, Y. *et al.* Morphing pasta and beyond. *Sci. Adv.* **7**, eabf4098 (2021).
58. Lutz-Bueno, V., Bolisetty, S., Azzari, P., Handschin, S. & Mezzenga, R. Self-winding gelatin–amyloid wires for soft actuators and sensors. *Adv. Mater.* **32**, 2004941 (2020).
59. Czerner, M., Fellay, L. S., Suárez, M. P., Frontini, P. M. & Fasce, L. A. Determination of elastic modulus of gelatin gels by indentation experiments. *Procedia Mater. Sci.* **8**, 287–296 (2015).
60. Quan, H., Pirosa, A., Yang, W., Ritchie, R. O. & Meyers, M. A. Hydration-induced reversible deformation of the pine cone. *Acta Biomater.* **128**, 370–383 (2021).
61. Elbaum, R., Zaltzman, L., Burgert, I. & Fratzl, P. The role of wheat awns in the seed dispersal unit. *Science* **316**, 884–886 (2007).
62. Armon, S., Efrati, E., Kupferman, R. & Sharon, E. Geometry and mechanics in the opening of chiral seed pods. *Science* **333**, 1726–1730 (2011).
63. Taccola, S. *et al.* Toward a new generation of electrically controllable hygromorphic soft actuators. *Adv. Mater.* **27**, 1668–1675 (2015).
64. Kang, H., Lee, M., Lim, H., Stone, H. A. & Lee, J. Hygromorphic actuator from a metal oxide film driven by a nano-capillary forest structure. *NPG Asia Mater.* **9**, e417–e417 (2017).
65. Ma, M., Guo, L., Anderson, D. G. & Langer, R. Bio-inspired polymer composite actuator and generator driven by water gradients. *Science* **339**, 186–189 (2013).
66. Okuzaki, H., Kuwabara, T. & Kunugi, T. Theoretical study of sorption-induced bending of polypyrrole films. *J. Polym. Sci. Part B Polym. Phys.* **36**, 2237–2246 (1998).
67. Green, D. W., Winandy, J. E. & Kretschmann, D. E. *Mechanical properties of wood*. 4.1-4.45 https://www.fs.usda.gov/treesearch/pubs/7149 (1999).
68. Chen, Z., Majidi, C., Srolovitz, D. J. & Haataja, M. Tunable helical ribbons. *Appl. Phys. Lett.* **98**, 011906 (2011).

Supplementary Videos

Video S1: Natural *Erodium* seed has an inevitable crevice searching phase that can negatively impact the drilling efficiency especially for relatively flat land. (VideoS1_Natural seed drilling.mp4)

Video S2: Dropping test of both natural and engineered seed carriers. Compared to *Erodium* seeds which have an 80% chance to land flat, this three-tailed carrier has a 90% chance of landing with an ensured angle between its body and ground to increase the drilling success. (VideoS2_Dropping test.mp4)

Video S3: Comparing the self-drilling success of the engineered three-tail seed carrier and the natural single-tail *Erodium* seed. (VideoS3_Compare three tail drilling to natural seed drilling.mp4)

Video S4: Experiment and finite element simulation of the uncoiling and self-drilling processes of both three-tailed and single-tailed designs. Three-tailed design generates larger force as multiple tail tips and bodies can generate effect torques simultaneously. **(**VideoS4_Finite element simulation.mp4)

Video S5: Self-drilling processes of three seed carrier design variations including three-tailed, double-coiled and large-sized systems, tailored to different use cases. The tests were conducted in an indoor controlled environment. (VideoS5_Three design variations.mp4)

Video S6: Fabrication process of the seed carriers. (VideoS6_Fabrication process.mp4)

Video S7: Germination experiment of three-tail seed carrier with embedded symbiotic cherry belle radish seeds and beneficial fungi, captured for a duration of 190 hours. (VideoS7_Fungi and seed.mp4)

Video S8: Successful self-drilling and germination under natural conditions outdoor for seven continuous days, with two intermittent light rains on the first day and one thunderstorm and heavy rain lasted for more than six hours on the second day. (VideoS8_Outdoor drilling and germination.mp4)

Supplementary Files

This is a list of supplementary files associated with this preprint. Click to download.

- VideoS2Droppingtest.mp4
- VideoS4Finiteelementsimulation.mp4
- VideoS7Fungiandseed.mp4
- VideoS8Outdoordrillingandgermination.mp4
- VideoS5Threedesignvariaions.mp4
- VideoS1Naturalseeddrilling.mp4
- VideoS6Fabricationprocess.mp4
- VideoS3Comparethreetaildrillingtonaturalseeddrilling.mp4